

HAC REF G4663

2

AD-A242 747



DTIC
ELECTE
NOV 22 1991
S C D

HIGH TEMPERATURE SUPERCONDUCTOR THIN FILMS AND JOSEPHSON JUNCTIONS

A.T. HUNTER

Hughes Research Laboratories
3011 Malibu Canyon Road
Malibu, California 90265

October 1991

Final Report
Contract N00014-88-C-0667
September 1988 through August 1991

OFFICE OF NAVAL RESEARCH
Department of the Navy
800 N. Quincy Street
Arlington, VA 22217-5000

91-15315



REPORT DOCUMENTATION PAGE

Form Approved
OMB No. 0704-0188

1a. REPORT SECURITY CLASSIFICATION UNCLASSIFIED		15. RESTRICTIVE MARKINGS	
2a. SECURITY CLASSIFICATION AUTHORITY		3. DISTRIBUTION / AVAILABILITY OF REPORT	
2b. DECLASSIFICATION / DOWNGRADING SCHEDULE			
4. PERFORMING ORGANIZATION REPORT NUMBER(S)		5. MONITORING ORGANIZATION REPORT NUMBER(S)	
6a. NAME OF PERFORMING ORGANIZATION Hughes Research Laboratories	6b. OFFICE SYMBOL <i>(If applicable)</i>	7a. NAME OF MONITORING ORGANIZATION Office of Naval Research	
6c. ADDRESS (City, State, and ZIP Code) 3011 Malibu Canyon Road Malibu, CA 90265		7b. ADDRESS (City, State, and ZIP Code) Department of the Navy 800 N. Quincy Street Arlington, VA 22217-5000	
8a. NAME OF FUNDING / SPONSORING ORGANIZATION DARPA	8b. OFFICE SYMBOL <i>(If applicable)</i>	9. PROCUREMENT INSTRUMENT IDENTIFICATION NUMBER N00014-88-C-0667	
8c. ADDRESS (City, State, and ZIP Code) 1400 Wilson Blvd. Arlington, VA 22209		10. SOURCE OF FUNDING NUMBERS	
		PROGRAM ELEMENT NO.	PROJECT NO.
		TASK NO.	WORK UNIT ACCESSION NO.
11. TITLE (Include Security Classification) High Temperature Superconductor Thin Films and Josephson Junctions			
12. PERSONAL AUTHOR(S) Hunter, A.T.			
13a. TYPE OF REPORT Final	13b. TIME COVERED FROM 88/9 TO 91/8	14. DATE OF REPORT (Year, Month, Day) 91/10/31	15. PAGE COUNT 51
16. SUPPLEMENTARY NOTATION			
17. COSATI CODES		18. SUBJECT TERMS (Continue on reverse if necessary and identify by block number)	
FIELD	GROUP	SUB-GROUP	
19. ABSTRACT (Continue on reverse if necessary and identify by block number)			
<p>We have developed processes for the sputter deposition and device fabrication of Josephson tunneling structures made from YBCO materials. Very high critical current density YBCO films were used to make several different types of weak link structures. An 8-nm-diam focused ion beam was used to pattern thin YBCO films by implant damage. Procedures to fabricate trilayer devices utilizing a-axis films and non-superconducting YBCO barriers were developed. Superconducting transport through the barrier was observed, but was limited by base-electrode critical current density. These results indicated to us that edge-junctions would be better suited to the relatively low resistance barriers than are trilayer junctions. In the final stages of the program, we developed procedures for fabricating all YBCO edge junctions. Using a post annealed base electrode and <i>in situ</i> counter electrode and no deposited barrier, we measured junction current densities up to 10^6 A cm⁻², demonstrating</p>			
20. DISTRIBUTION / AVAILABILITY OF ABSTRACT <input type="checkbox"/> UNCLASSIFIED / UNLIMITED <input checked="" type="checkbox"/> SAME AS RPT. <input type="checkbox"/> DTIC USERS		21. ABSTRACT SECURITY CLASSIFICATION	
22a. NAME OF RESPONSIBLE INDIVIDUAL Dr. Kristal B. Hathaway Code 1114ss		22b. TELEPHONE (Include Area Code) (703) 696-4508	22c. OFFICE SYMBOL

19. (cont'd)

successful implementation of the steps required to make edge junctions, including successful annealing of the ion milling damage at the edge during counter electrode growth. This result indicates that barriers are not formed as uncontrolled artifacts of edge-junction processing, and is a crucial test of the feasibility of fabricating edge junctions with reproducible, controlled properties using deposited barriers. Edge-junction devices were fabricated with a 10-nm non-superconducting YBCO barrier under the superconducting counter-electrode layer. In these devices, the junction critical current was controlled by the barrier material. We observed significant suppression of the critical current by RF radiation, an indication of the successful demonstration of an all-YBCO tunneling device.

CONTENTS

		Page
1	INTRODUCTION	1
	1.1 Relevance to DoD Systems.....	1
	1.2 Goal of Program.....	1
	1.3 Program Approach	1
	1.4 Key Results	2
	1.5 Outline of Report.....	3
2	MATERIALS ISSUES.....	4
	2.1 Sputter Deposition.....	4
	2.2 Processing Issues.....	7
3	FIB PATTERNING OF YBCO FILMS.....	10
	3.1 Focused Ion Beam System.....	10
	3.2 Approaches to Weak-Link Formation.....	10
	3.3 Normal-Metal Bridge Approach	10
	3.4 Gap Approach	16
4	TRILAYER RESULTS	28
	4.1 Approach to Junction Formation.....	28
	4.2 Electron Characteristics of Processed Devices	28
5	EDGE JUNCTIONS	32
	5.1 Approach to Edge-Junction Formation	32
	5.2 Device Characteristics With No Deposited Barrier	32
	5.3 Device Characteristics With Deposited Barrier	38
6	SUMMARY AND CONCLUSIONS.....	43

Statement A per telecon
 Dr. Kristl B. Hathaway ONR/Code 1114
 Arlington, VA 22217-5000

NW 11/22/91

Accession For	
NTIS GRA&I	<input checked="" type="checkbox"/>
DTIC TAB	<input type="checkbox"/>
Unannounced	<input type="checkbox"/>
Justification	
By	
Distribution/	
Availability Codes	
Dist	Special
A-1	



ILLUSTRATIONS

		Page
1	Normalized Room Temperature Conductivity of an Initially 120-nm-thick film of YBCO as a function of ion-milling time, where the conductivity is defined as unity before milling starts	8
2	AC Magnetization Scans for Initially 120-nm-Thick Films of YBCO at Various Stages of the Thinning Process	9
3	Cross-section Showing a Procedure Used for Making Weak Links in Thin Films of YBCO	11
4	Geometry of the Experiment Used to Determine the Effect of the Ga Focused Ion Beam on the Transport through Photolithographically Defined YBCO Lines...	13
5	YBCO Line Resistance as a Function of Temperature at Various Stages of Processing.....	14
6	Conductance (dI/dV) as a Function of Voltage Drop for the Superconducting-Normal-Superconducting Structure Made With a Au Bridge Across a Region Damaged With Dose of 1×10^{16} cm^{-2} Ga Ions, Showing the Structure is Non-Linear at Low Temperatures, but resistive at temperature of 54K.....	16
7	Scanning Electron Micrograph of the 100-nm-Thick Au Bridge Spanning the Damaged YBCO After a $600^\circ\text{C}/0.5$ h Anneal	17
8	Cross-Sectional and Top Views of the Procedure Used to Make Weak Links From Photolithographically Defined Lines in YBCO.....	18
9	Current-Voltage Characteristics Measured at 49K for Eight Different 5- μm -Thick Lines Patterned in a 60-nm-Thick YBCO Film.....	20
10	Critical Current Density for a 5- μm -Wide Line Patterned in a 60-nm- Thick YBCO Film Before (Circles, Upper Set of Points) and after (Squares, Lower Set of Points) Patterning With a Focused Ion Beam.....	21
11	TRIM Calculation (J.F. Ziegler, IBM) Showing the Concentration of Ga (Triangles) as a Function of Depth for a 50-kV Ga Ion Beam in YBCO	22
12	AC Magnetization Scans as a Function of Temperature for Thin Post- Annealed YBCO Films Used for Focused Ion Beam Damage Experiments	23
13	Current-Voltage Characteristics for 4 Different 5- μm Wide Lines, and 2 Devices Consisting of two 5- μm Wide Lines in Parallel, Patterned From a 20-nm Thick Post-Annealed YBCO Film Showing Excellent Uniformity and High Current Density Before FIB Exposure	24
14	Current-Voltage Characteristics for a 5- μm Wide Line Patterned in a 20-nm Thick Post-Annealed YBCO film, at Various Stages of Processing.....	26
15	Diagram Showing the Steps Taken to Pattern Trilayer Samples Into Junctions.....	29
16	Microphotograph of Fully Processed all-YBCO Trilayer Junction	30
17	Critical Current for Three Different Sized Trilayer Junctions as at Function of Junction Length, Measured at 4.5K	31
18	Diagram of One Cell of the Mask Set Used to Make Edge Junctions From YBCO Films.....	33

ILLUSTRATIONS (Continued)

		Page
19	Diagram Showing the Procedure Used to Fabricate Edge Junctions From YBCO Films.....	34
20	Microphotograph of a Fully Processed All YBCO Edge Junction SQUID (Left Hand Picture) Showing Details of 10- μ m Wide Counter Electrode Line Contacting Base-Electrode Edge (Right Hand Picture)	35
21	AC Magnetization as a Function of Temperature for an Edge Junction Sample.....	37
22	Critical Current Density as a Function of Temperature for Test Patterns Fabricated From the Edge Junction Mask Set Made From the Base-Electrode Materials (Circles) or the Counter- Electrode Material (Triangles).....	39
23	AC Magnetization as a Function of Temperature for Two Post-Annealed YBCO Base-Electrode Layers.....	40
24	AC Magnetization as a Function of Temperature for an Edge Junction Sample at Two Stages of Processing	41
25	Critical Current as a Function of Temperature for Patterns on an Edge Junction Sample made with a 10-nm Non-Superconducting Barrier and a 140-mA <i>in situ</i> Counter Electrode.....	42

1. INTRODUCTION AND OVERVIEW

1.1 RELEVANCE TO DoD SYSTEMS

High-speed and low-power-dissipation electronics have many applications of potential interest to the Department of Defense. Superconducting-based circuits offer promise particularly for applications already requiring cryogenic cooling. An example would be signal processing electronics for infrared detector focal plane arrays. The recent advent of high temperature superconductors with transition temperatures well above the boiling point of liquid nitrogen offers substantially increased operating temperatures for such cryogenic circuitry. Higher operating temperatures than are achieved with Nb or NbN circuits could change the systems trade-offs in a way that would greatly expand the range of applications where such circuits could be used to advantage.

The fundamental building blocks for superconducting circuits are Josephson junctions. A major technical challenge lies in fabricating Josephson junctions from high temperature superconductors. However, realization of system benefits from this new technology requires more than demonstrating that such devices are possible and have properties required by the application. The development of production-worthy fabrication procedures is in the long run crucial for the actual implementation of this new technology.

1.2 GOAL OF PROGRAM

The principal goal of this program was the development of film deposition and device processing techniques leading to the fabrication of an all-YBCO Josephson junction, thus establishing a basis on which to develop a superconducting circuit technology.

1.3 PROGRAM APPROACH

This report summarizes our technical progress towards the development of all $\text{YBa}_2\text{Cu}_3\text{O}_x$ (YBCO) Josephson tunneling junctions. We selected YBCO over the Bi or Tl based systems with higher transition temperatures because it appeared difficult to stabilize the high transition temperature phases of those other systems, and the path towards *in situ* growth (crystallization during deposition) was feasible for YBCO.

We worked exclusively with thin films of YBCO deposited using simultaneous co-sputtering using separate targets to independently control the amount of Y, Ba, and Cu present in the films. This approach was chosen because it appeared to have substantial potential for manufacturability because of relatively high deposition rates and large-area uniform coverage.

Several approaches leading towards the fabrication of Josephson devices are detailed in this report. Our intent at the outset of this program was to work towards sandwich style junctions

with YBCO base and counter electrodes by a series of intermediate steps involving devices with low T_c counter electrodes. As time progressed it became apparent that we could gain more relevant experience by dealing only with all-YBCO structures. We started with focused ion beam (FIB) patterning of thin YBCO films to learn about YBCO processing in a way that could yield an operating YBCO weak link, then progressed to fabricating all YBCO sandwich or edge-geometry junctions.

1.4 KEY RESULTS

Thin film properties we have demonstrated greatly exceed our expectations at the beginning of this program. Post-annealed films used in this program are highly c-axis oriented on either SrTiO_3 or LaAlO_3 substrates, with transition temperatures exceeding 90 K and with transition widths (defined as the 10 to 90% shielding transition in an AC magnetization experiment) of less than 0.3°K . Critical current densities for post annealed films routinely exceed 10^6 A cm^{-2} , in some cases reaching this value above 77 K. We successfully grew and patterned post-annealed films as thin as 20 nm. These 20-nm films had transition temperatures above 70 K, and critical current densities exceeding $3 \times 10^6 \text{ A cm}^{-2}$ at 24 K. While these extremely high-quality post-annealed were extensively used for certain of our weak-link approaches, *in situ* films are better suited to multilayer structures. The best *in situ* films used for this program have critical current densities in excess of 10^6 A cm^{-2} at low temperatures (below 20 K for the counter electrode layer of one edge junction sample), but do not have transition temperatures as high as the post annealed samples. Transition temperatures for most of the *in situ* films used for devices in this program varied from 50 to 60 K. In related IR&D work, we were able to deposit single *in situ* films that had transition temperatures as high as 86 K, showing the potential of the sputtering technique to produce high quality films that are superconducting as deposited.

We investigated the use of a gallium FIB for very high resolution patterning of thin films of YBCO. We concluded that direct writing into the YBCO using implantation damage was the most effective method of preserving the very high resolution of the 8-nm-diameter beam. We observed non-linear current voltage characteristics for superconducting-normal-superconducting structures made by bridging heavily implanted (10^{15} cm^{-2}) damage tracks with Au. For very thin films (20 to 40 nm, matched to the range of 50 kV Ga in YBCO), we were able to reduce critical currents with a single pass of the beam at doses below 10^{14} cm^{-2} , and make the material resistive at this dose and above.

We successfully fabricated all-YBCO trilayer structures that utilized non-superconducting YBCO barriers. For either 10- or 50-nm-thick barriers, we found that the structure critical current was limited by the current density of the base electrode layers rather than that of the

junction. This was largely a consequence of the device geometry and the relatively low barrier resistance provided by non-superconducting YBCO.

The edge-junction geometry is more favorable for low resistance barriers because the junction area can be made small. We designed an edge junction mask set, developed the processing tools necessary to fabricate YBCO edge junctions, and processed several lots of all YBCO edge junctions. For devices made with no deliberate barrier, we achieved junction critical current densities at or above 10^6 A cm⁻², limited by the *in situ* counter electrode transport properties. This result demonstrates that we have all the processing tools required for edge junction fabrication, and indicates successful annealing of the ion milling damage at the base-electrode edge during the counter-electrode deposition, a crucial test of the feasibility of this approach. The final edge-junction structures fabricated for the program utilized a 10-nm-thick non-superconducting YBCO barrier under the counter-electrode layer. Junction critical current densities in this case were substantially reduced from those measured for the counter electrode, indicating successful fabrication of weak links. The junctions showed substantial critical current suppression on exposure to RF frequencies, an indication of superconducting tunneling at the junction.

1.5 OUTLINE OF REPORT

The report is composed of four sections on technical progress, which are followed by a section summarizing our progress and suggesting directions that would build on the work done under this program to make further progress towards reliable fabrication of Josephson devices. The first section below deals in broad terms with material issues relevant to device fabrication. This section primarily discusses development of YBCO film deposition for junctions, and contains information on etching and thinning experiments applicable to thin film devices in general. The next three sections deal with progress towards fabrication of specific types of Josephson devices. More detailed deposition and processing information is contained in these sections where it applies specifically to one type of device. The first of the device sections discusses our use of a focused beam of Ga ions to make very high resolution patterns in thin YBCO films. The next device section covers results on trilayer junctions formed with non-superconducting YBCO barriers. The results of this work strongly motivate efforts described in the last device section directed towards fabrication of all-YBCO edge junctions.

2. MATERIALS ISSUES

This section outlines work done to refine material deposition and processing steps needed for the development of weak link junctions. We were able to benefit from work done on our Independent Research and Development (IR&D) "High Temperature Superconductors" project. The objectives of the IR&D project included more general research aimed at understanding the sputter deposition growth process, as well as chemistry of YBCO relevant to processing. Additional work needed to apply what was learned on the IR&D project specifically to junction fabrication was included in this program, and is described below. We will also summarize aspects of the IR&D research where they have a strong bearing on junction fabrication. Our progress in sputter deposition, using both a post-annealed and an *in situ* process, is described. Processing issues we discuss include etching procedures, ion thinning, and effects attributable to oxygen loss during processing.

2.1 SPUTTER DEPOSITION

We chose to focus on a single deposition technique for all of our high temperature superconductivity work. The technique we chose was simultaneous co-sputtering. The advantages we gain from this method include uniformity over large areas (the system was designed to accommodate 3 inch diameter substrates, although we typically used 2 inch diameter LaAlO₃ substrates, the largest ready available), and relatively high deposition rates.

The deposition system was custom built by Perkin-Elmer, and includes two independent sputtering chambers, each with three 4-inch diameter magnetron targets. One of the three targets uses an RF power supply, allowing for the deposition of non-conducting metal oxides or dielectrics. The other two magnetron targets in each chamber are powered by DC supplies and are designed for metal deposition. The post-annealed films discussed below were deposited with Y, Cu, and BaF₂ targets, with the substrate at ambient temperature and without added oxygen in the deposition chamber. Deposition of *in situ* films utilized Y and Cu targets to provide independently adjustable sources of those metals, while a Ba_{0.5}Cu_{0.5} target supplied the Ba. The substrate holder is located off the axis of the sputtering targets to help minimize resputtering of the growing film by negative ions from the targets. The substrate holder is positioned on a rotatable substrate stage, and a gas ring positioned near the substrate can be used to supply extra oxygen during film deposition. The heater used to warm the substrate during growth is discussed in some detail below.

Accurate calibration of sample stoichiometry is probably the biggest challenge presented by this deposition technique. While independent control of the three different targets allows precise control of sample stoichiometry, the individual sputter rates depend on conditions of the target

including degree of oxidation. This means in practice that sputter rates must be recalibrated after venting the system to air, and periodically during use of the targets.

For post-annealed samples where the depositions were done at ambient temperature, this calibration could be very accurately done by forming thin films on Si, then determining the metal ratios by Rutherford back scattering (RBS).

For *in situ* growth, where the substrate is at an elevated temperature, it is more difficult to obtain a good calibration. The stoichiometry is altered as the substrate temperature is raised. At the oxygen partial pressures and temperatures used for our growth, we believe that this is largely due to the temperature variation in the sticking coefficient of the metallic Cu present at the surface. Because YBCO reacts with Si at the elevated temperatures required for *in situ* growth, we were unable to use RBS analysis of YBCO films on Si to calibrate our *in situ* growths. Instead, we had to rely on determining the stoichiometry for a low temperature deposition, then making adjustments to the Cu sputtering rate to get the proper stoichiometry at higher substrate temperatures. We used SEM and x-ray evaluation of secondary phases and transition temperature as guides in making these adjustments.

We evaluated some other techniques to provide the needed calibration, but did not find one that worked better than the approach described above. Auger analysis was probably the most promising alternative technique investigated, but we found that the yields for the different constituents depended too much on oxidation state to make this a reliable technique.

We initially used SrTiO₃ substrates for depositions used in this program. For these films, we deposited films onto SrTiO₃ substrates at ambient temperature using co-sputtering with separate Y, Cu, and BaF₂ targets, and without adding extra oxygen to the deposition chamber. After annealing at 850°C in wet oxygen, the films are superconducting with zero resistivity above 90 K. The films are highly oriented, with a mixture of c- and a-axis material. One film of this type, used for initial focused ion beam experiments, is CS181. This film had a very sharp resistive transition, falling 3 orders of magnitude in 1 K, to below 10⁻⁸ Ω-cm at 88 K. Bridges were defined on this film with CW laser patterning, and current-voltage characteristics were measured to determine critical current. We used a voltage criterion of 1 × 10⁻⁷ V, leading to an electric field criterion of 2 × 10⁻⁵ V-cm⁻¹ for the critical current density for our 50 μm long patterns. We plan to define longer bridges to allow use of the recommended electric field criterion of 1 × 10⁻⁶ V-cm⁻¹ in the future. We have also done a careful analysis of the functional dependence of voltage on current for these shorter bridges. Fitting our data to $V = \alpha I^n$ (where V is voltage, I is current, and α and n are fitting parameters) in the region between 10⁻⁷ and 10⁻⁶ V yields values of n in zero applied magnetic field that range between 57 at 53.1 K to 24 at 77.8 K. If this dependence holds at lower values of voltage, we would expect an electric field criterion of 10⁻⁶ V-cm⁻¹ to reduce the calculated current density by only 12% at 77.8 K, and less

at lower temperatures. Therefore, we conclude that the values of critical current as determined from this short bridge are meaningful. Critical current densities determined as described above ranged from 6.5×10^6 A-cm⁻² at 53.1 K to 1.3×10^6 A-cm⁻² at 77.8 K. The critical current density at 53.1 K was still above 10^6 A-cm⁻² (1.5×10^6 A-cm⁻²) in an applied field of 0.37 Tesla.

We switched to LaAlO₃ substrates later in the program, since they were available in larger diameter. The relatively low dielectric constant and loss tangent of LaAlO₃ substrate material make it usable for high frequency passive components, so much of our initial efforts to produce high quality films on these substrates was done as part of our IR&D project, and our results are summarized here. We found that with the proper substrate preparation and annealing treatment, we could get critical temperature and current properties comparable to those discussed for the films on SrTiO₃. A preanneal of the LaAlO₃ substrates in dry O₂ was found to improve the morphology of YBCO films deposited onto the substrates, presumably due to removal of polishing defects on the LaAlO₃ surface. Most of the post-annealed films used for this program were done under the following conditions: 850°C anneals for approximately 0.5 hr in 1 atm O₂ saturated (at room temperature) with H₂O. In our IR&D project we found that lower oxygen partial pressures lead to improved electronic properties, and that higher temperature, but briefer anneals could improve film morphology, especially for very thin films (20 to 40 nm). Conditions used to obtain these improved properties will be discussed below under sections devoted to the devices or structures utilizing the films.

Progress on *in situ* deposition was mainly determined by progress towards developing an optimized substrate heater. The issues are well known, and primarily involve designing a heater capable of reliable high temperature operation in the presence of 1 to 10 mTorr of oxygen. Since uniform deposition involves substrate rotation, we relied on radiative heating of the LaAlO₃ substrates. This in turn requires very high temperatures for the heater, as well as development of an effective infrared absorber for the back of the LaAlO₃ substrate.

Three different substrate heaters were used during the course of this program, and eventually led to a system capable of heating the substrates to 800°C in the presence of O₂ with a reasonable lifetime. The substrate holder delivered with the system in 1988 utilized a tungsten-wire heater, which was inappropriate for depositions requiring partial pressures of oxygen. A modified Pt-Rh wire wound heater was designed and received at the end of 1989. After further modification to add a second layer of wire, we achieved temperatures of 750°C in both 100 m Torr of N₂ and in air, temperatures needed for *in situ* growth in highly oxidizing environments.

We used this modified substrate heater to deposit films at substrate temperatures of up to approximately 650°C in an oxygen partial pressure, using Y, Cu and BaCu targets. Post deposition annealing of these wafers at 650°C in oxygen produced extremely smooth superconducting films with somewhat reduced (~65 K) transition temperatures. Using the same

heater, we were able to achieve somewhat higher substrate temperatures (up to 700°C) by coating the back of the LaAlO₃ wafers with an infrared absorbing material. We deposited films with transition temperatures as high as 75 K after a low temperature 650°C anneal in oxygen. The films are very smooth and are highly c- or a-axis oriented.

Temperatures achievable with the wire wound heater were not sufficient for optimized *in situ* films, and the lifetime of the heater is limited. The lifetime at even 650°C substrate temperature was limited to several hours. The third and final iteration of heater design involved use of a pyrolytic boron nitride encapsulated graphite heater. The pyrolytic BN protects the graphite very effectively from oxygen, the heater is capable of very high temperatures, and the thermal expansion properties of the graphite and BN are matched closely enough to ensure good adhesion over many temperature cycles. Substrate temperatures of up to 800°C in 5 mTorr oxygen were achieved, which resulted in films with transition temperatures up to 86 K. Deposition rates under these deposition conditions were of the order of 200 nm per hour.

2.2 PROCESSING ISSUES

The stoichiometric removal of material by Br etching makes this a possibly attractive technique to form gaps in YBCO bridges for the formation of SNS structures, or for cleaning ion-milled edges before barrier and counter-electrode deposition for edge junctions. We investigated the etch rates of Br in ethylene glycol. This solvent was used because, unlike methanol, it does not dissolve certain types of photoresist, providing the potential for a wider use of the etch. We etched a series of steps in films of YBa₂Cu₃O₇ and used SEM images to determine the amount of superconductor removed. The etch is apparently highly selective to YBa₂Cu₃O₇. Etch rates vary considerably depending on the morphology of the films, presumably because of the presence of secondary phases that etch more slowly than YBa₂Cu₃O₇. The films used for this investigation were nominally 100 nm c-axis oriented films on LaAlO₃. Between 80 and 120 sec were required to fully etch the 100 nm films in an 0.5% Br solution at ambient temperature.

We found Ar-ion milling to be an effective method of patterning YBCO layers, as well as insulators such as MgO used in edge-junction and trilayer processing. With a 500 V beam voltage and a beam current of 0.6 A cm⁻², we typically achieved milling rates of approximately 23 nm per minute.

Ion milling to locally thin regions of films to be subsequently modified by the FIB offers the advantage of leaving contacts and other parts of the film thicker, and therefore somewhat more robust. We started with a superconducting film 120 nm in thickness and milled it with a 500 V Ar beam. The sample was tilted so that the beam impinged on the surface at 80° to the sample normal to minimize damage caused by Ar penetration into the film. We used room temperature conductivity as a monitor of amount of material removed. Figure 1 shows normalized

conductivity for the film at room temperature (which we take as proportional to the film thickness) as a function of milling time. The apparent milling rate slows from approximately 20 nm/min to ~8 nm/min after approximately half the film has been removed. At less frequent intervals we used AC magnetization to assess the superconducting properties of the film as it is milled. Figure 2 shows these data. The transition midpoint moves from 86 K for no milling, to ~69 K for 345 sec of milling. After 345 sec of milling we estimate the film was approximately 42 nm thick from the room temperature conductivity.

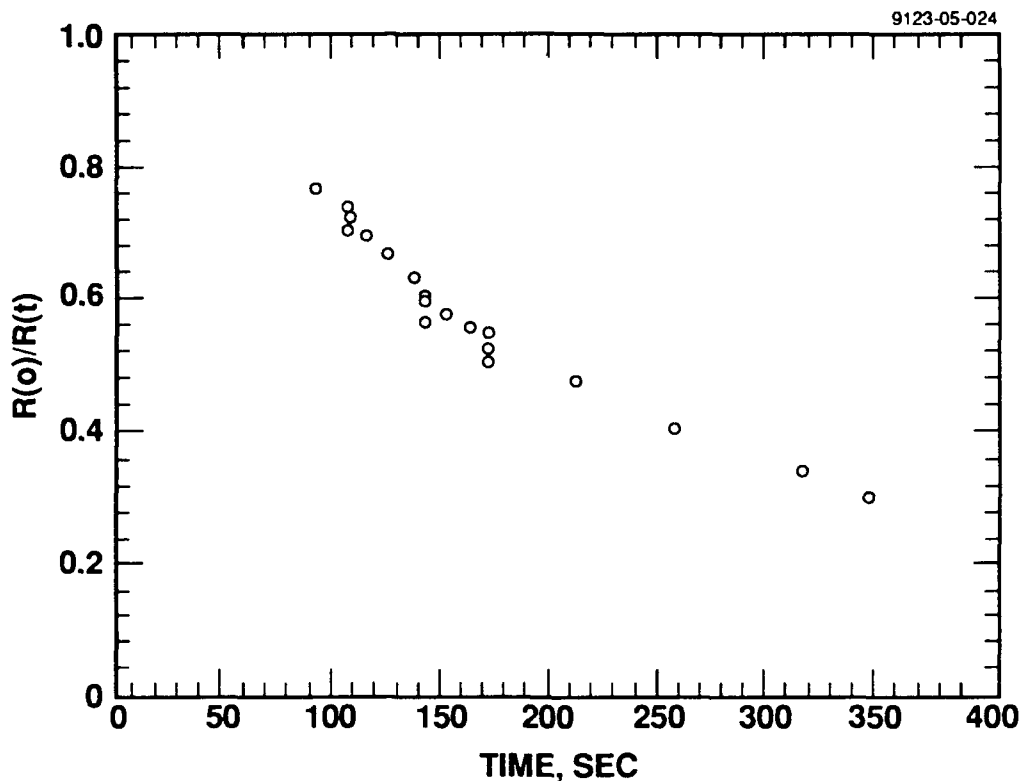


Figure 1. Normalized room temperature conductivity of an initially 120-nm-thick film of YBCO as a function of ion-milling time, where the conductivity is defined as unity before milling starts.

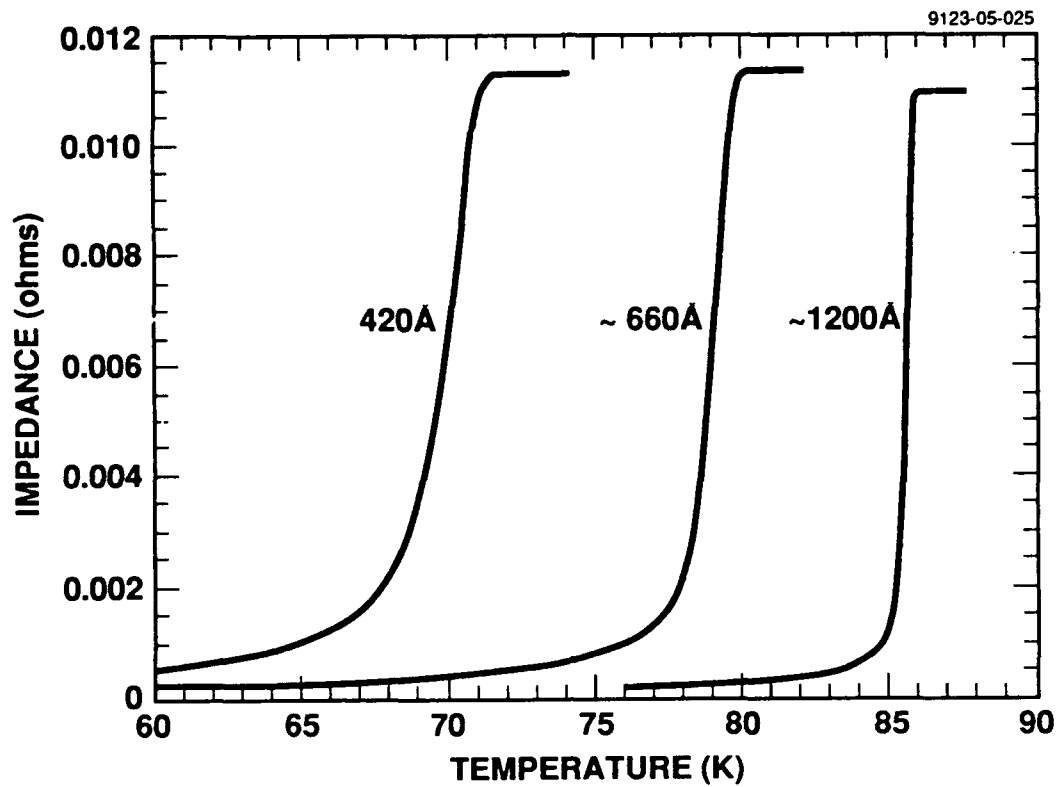


Figure 2. AC magnetization scans for an initially 120-nm-thick films of YBCO at various stages of the thinning process. The film thickness is indicated for each scan, and was estimated from the room temperature conductivity.

3. FIB PATTERNING OF YBCO FILMS

3.1 FOCUSED ION BEAM SYSTEM

The 50-keV focused-ion-beam system used for this work was built in-house and formed a focused spot image of the virtual ion source on the target plane at a magnification of either 0.14 or 0.08. The system consisted of a single isotope liquid-metal gallium ion source, two electrostatic lenses, a pair of octopole deflectors positioned above the final lens elements, a beam blanker, and associated video, deflection, and pattern generation electronics. The spot diameter and target current were 15 nm and 10 pA, respectively, for the system configured at a magnification of 0.14. At the lower magnification of 0.08, the spot diameter and target current were 8 nm and 1.5 pA, respectively. The latter performance represents the best resolution ever achieved with a focused beam of ions.

3.2 APPROACHES TO WEAK-LINK FORMATION

We investigated several ways of utilizing the extremely high resolution of the FIB system to make weak links in YBCO films. The first approach involved using the beam to expose very thin lines in PMMA photoresist and transfer the pattern into the YBCO by etching. The transfer process decreased the resolution attainable with the beam. This observation motivated use of beam damage to write lines directly into the YBCO. We then went on to make superconducting-normal-superconductor (SNS) structures either by bridging the damaged region with Ag or Au, or by leaving a narrow gap of normal YBCO that could be driven normal by current biasing.

We have successfully made 50 to 100 nm groves in PMMA on $\text{YBa}_2\text{Cu}_3\text{O}_7$. Transfer of the narrow groves formed in photoresist into $\text{YBa}_2\text{Cu}_3\text{O}_7$ results in a serious increase of the groove width. Ion milling for pattern transfer is not usable because of the thin layer of photoresist required for the FIB exposure, and the relatively slow milling rate for $\text{YBa}_2\text{Cu}_3\text{O}_7$. Wet etching with the Br-ethylene glycol etch results in several hundred nanometer lines. These experiments indicated that instead of pattern transfer, we should emphasize direct writing on the $\text{YBa}_2\text{Cu}_3\text{O}_7$, using ion-beam damage to make patterns in the $\text{YBa}_2\text{Cu}_3\text{O}_7$.

3.3 NORMAL-METAL BRIDGE APPROACH

Figure 3 illustrates the next approach towards SNS weak-link formation using focused ion beam damage. We photolithographically defined 5 μm wide lines in the YBCO, which were then damaged all the way across using the high resolution Ga FIB. Normal metal (Ag or Au) was used to bridge the damaged regions to make SNS structures. We review below the experiments we did to investigate the metal superconductor interface, and to determine the dose necessary to make the damaged YBCO non-superconducting.

9023-05-01

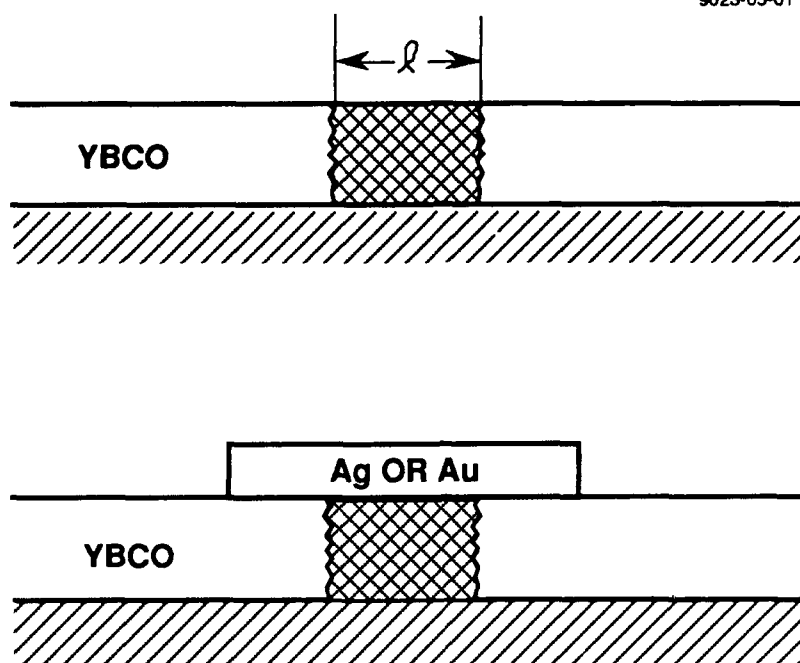


Figure 3. Cross-section showing a procedure used for making weak links in thin films of YBCO. A focused ion beam is used to damage the YBCO, which is then bridged with Ag or Au to make a superconducting-normal-superconducting structure.

We made three types of structures aimed at investigating the metal-superconductor interface, all on films grown on SrTiO_3 substrates: $\text{YBa}_2\text{Cu}_3\text{O}_7/\text{Au}$, $\text{YBa}_2\text{Cu}_3\text{O}_7/\text{MgO}/\text{Au}$, and $\text{YBa}_2\text{Cu}_3\text{O}_7/(\text{Ag or Au})/\text{Au}$. For the third structure, the Ag or Au was evaporated over the entire surface, then annealed at 525 or 625°C (for Ag or Au respectively). In all cases, the topmost Au was evaporated through a shadow mask to provide large contacts for the measurement of current-voltage characteristics.

For Au depositions onto bare $\text{YBa}_2\text{Cu}_3\text{O}_7$, the current-voltage characteristics were ohmic at low temperature, with contact resistances in the range of $10^{-5} \Omega\text{cm}^2$.

We investigated structures made by evaporating Au dots through a shadow mask onto YBCO films covered with 5 or 15 Å of sputtered MgO (CS105 or CS107, respectively). Neither sample showed evidence of tunneling. For the 5 Å sample, the impedance was almost purely capacitive. The capacitance measured for a 500 μm dot decreased monotonically with increasing temperature from 1.1 nF at 20 K to 0.6 nF at 100 K. The expected capacitance for 5 Å of MgO is approximately 33 nF, using the 90 K dielectric constant of 9.5. This result suggests that the

dielectric layer is much thicker than the 5 Å of MgO, and that a non-conducting interfacial region is present between the MgO layer and superconducting material lower in the $\text{YBa}_2\text{Cu}_3\text{O}_x$ film.

The results discussed above suggest that the surfaces of our $\text{YBa}_2\text{Cu}_3\text{O}_x$ films are not superconducting, a conclusion consistent with results from other groups. The last set of experiments were aimed at investigating whether the proximity effect can be exploited to overcome this problem. We deposited 10, 50 and 100 nm films of Ag and 50 nm films of Au on films of $\text{YBa}_2\text{Cu}_3\text{O}_x$. The wafers were then annealed to promote interdiffusion at the interface of the metal and superconductor, using 525°C/1 hr in O_2 for the Ag depositions, and 625°C/1 hr in O_2 for the Au. As an initial probe of the properties of these modified surfaces, we evaporated 500 μm -diameter Au dots through a shadow mask to define contacts, then made two wirebonds to each dot for testing. Our results for the proximity effect layers varied substantially from dot to dot on a given wafer, and between two identical wafers. However, our general conclusions are that the presence of the Ag proximity metal lowered the contact resistance by orders of magnitude in most cases; the Au to a lesser extent. These measurements indicate the need for annealing the normal metal bridges used in the SNS structures.

We have verified that FIB damage can be used as a patterning tool in our 60 nm thick films of $\text{YBa}_2\text{Cu}_3\text{O}_7$. Using our SNS-1 mask set, we fabricated 5 μm wide lines in 60 nm films and cut the lines with a single pass of a beam of Ga ions focused to 15 nm diameter. Figure 4 shows the geometry employed for the experiment.

In the first series of experiments using FIB damage, we wrote entirely across a 6 μm wide line in a 60 nm thick film grown on a SrTiO_3 substrate with one of the following five doses: 10^{12} , 10^{13} , 10^{14} , 10^{15} , and 10^{16} Ga cm^{-2} . A sixth line was left unimplanted for comparison. The two highest doses resulted in line resistances above $3 \times 10^5 \Omega$ (compared to a resistance of approximately $10^3 \Omega$ for an unimplanted line just above its transition temperature). Properties of lines implanted with doses of 10^{14} cm^{-2} or below were indistinguishable from the line with no implant. Annealing the sample at 500°C in O_2 (during a contact sintering step) reduced the resistance of the high impedance lines (approximately one order of magnitude for a 10^{16} cm^{-2} line measured before and after annealing), but the lines remained non-superconducting.

For two separate 6 bridge patterns we deposited 50 nm thick Ag or 100 nm thick Au bridges, respectively, across the implanted regions in an attempt to produce an SNS weak link. In the case of the Ag bridges, a 10 sec ion milling step was included just prior to Ag deposition and lift off as a cleaning step. Contact resistance between the film and the as-deposited Ag bridge was high, on the order or higher than $2.5 \times 10^{-1} \Omega \text{ cm}^2$. After annealing at 500°C in an oxygen atmosphere, the contact resistance was reduced to below $2.5 \times 10^{-4} \Omega \text{ cm}^2$, but current transport

9123-05-023

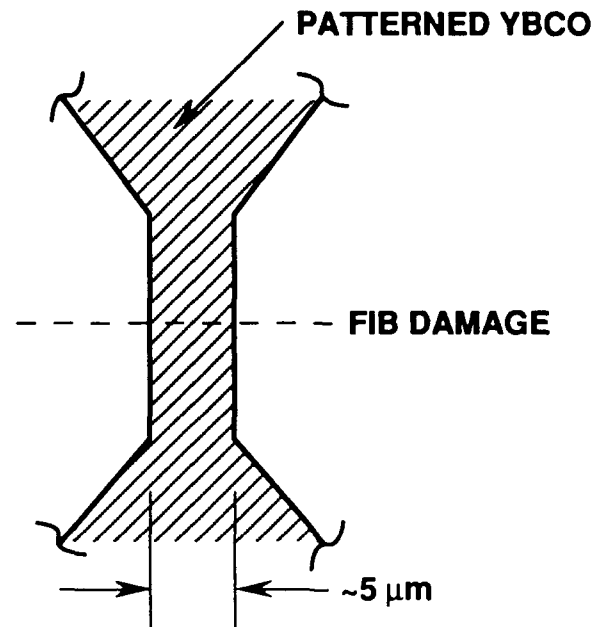


Figure 4. Geometry of the experiment used to determine the effect of the Ga focused ion beam on the transport through photolithographically defined YBCO lines. The YBCO line was damaged with a single pass of a 50 kV Ga beam as indicated in the figure.

was completely linear down to 300 A cm^{-2} , the lowest values of current density tested. Two different problem areas were identified for this approach. First, the electronic properties of the unimplanted 60 nm-thick YBCO bridge was degraded by the presence of the overlying Ag layer. Second, SEM images of the 50-nm-thick Ag dot used to bridge the implanted line show that the Ag "balled up" as a consequence of the 500°C anneal in O_2 , and was barely continuous. This means that the contact resistance inferred from the bridge resistance is probably overestimated, since the resistance of the Ag film is not negligible.

The result with the Au bridge was similar, although slightly more promising. Figure 5 summarizes our results for this sample. We have plotted bridge resistance at a particular value of current as a function of temperature to summarize the series of current-voltage curves measured for each bridge. The highest resistance bridge (curve 1 shows resistance vs temperature for this bridge) was implanted with $10^{16} \text{ Ga cm}^{-2}$. (The 10^{15} cm^{-2} bridge apparently had a higher resistance, and in fact was a fairly low leakage capacitor.) In comparison, the curves for the bridges with no implant and the 10^{14} cm^{-2} implant are superconducting, and are indistinguishable

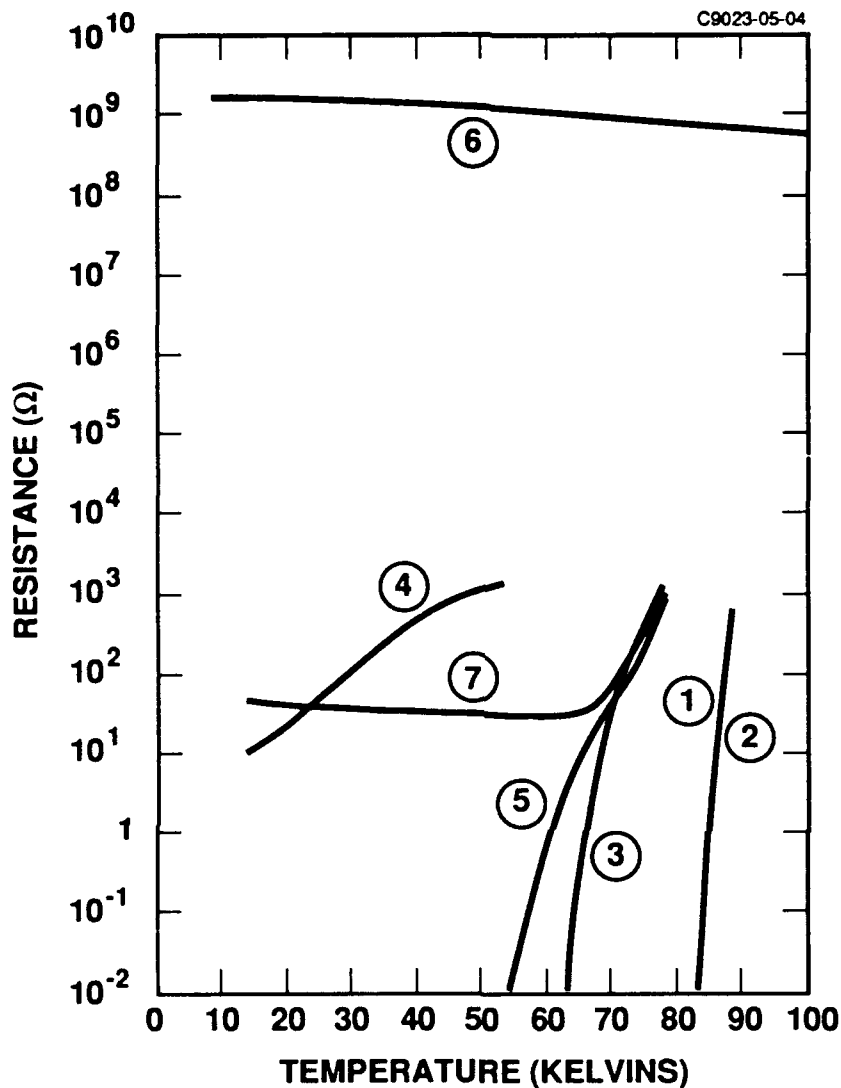


Figure 5. YBCO line resistance as a function of temperature at various stages of processing. 1) no implant, no anneal, 2) 10^{14} cm^{-2} , no anneal, 3) no implant, $500^\circ\text{C}/0.5 \text{ hr}$ anneal, 4) no implant, 500°C anneal, Au dot 5) no implant, $500^\circ\text{C}/0.5 \text{ hr}$ anneal, Au dot, $500^\circ\text{C}/0.5 \text{ hr}$ anneal, 6) 10^{16} cm^{-2} , no anneal 7) 10^{16} cm^{-2} , $500^\circ\text{C}/0.5 \text{ hr}$ anneal, Au dot, $500^\circ\text{C}/0.5 \text{ hr}$ anneal.

(these are the overlapping traces labelled 2 and 3 at the lower right of the figure, with resistance dropping below $10^{-2} \Omega$ at 84 K). After we annealed this sample at 500°C for 30 min in O_2 to lower contact resistance of the large contacts to the device, the transition temperature decreased by 20 K (shown by trace 4). We have investigated this deterioration of properties, and traced it to the use of a plasma oxidation step used to remove photoresist. (We have since then used acetone for photoresist removal instead of plasma oxidation and eliminated the problem.) We

used a lift-off process to pattern evaporated Au across the YBCO bridges, and used a brief Br-ethylene glycol etch before deposition as a clean up step. The ambient temperature deposition of the bridge metal even more dramatically reduced the transition temperature (curve 5), but in this case the pre-evaporation properties were substantially recovered upon annealing to 500°C in O₂ (curve 6). The resistance of the 10¹⁶ cm⁻² bridge with an annealed Au bridge across it is shown in curve 7. Unlike the case of the Ag bridges, the current-voltage characteristics of this bridge, as well as the Au bridge over the 10¹⁵ cm⁻² implant, were nonlinear. Figure 6 shows conductance (dI/dV) for the 10¹⁵ cm⁻² bridge plotted against voltage for a variety of temperatures. The nonlinearity vanishes at high enough temperature, indicating superconductivity may be involved in producing the nonlinearity. However, the zero voltage resistance is substantial, so that we are not seeing tunneling from superconductor on one side to that on the other. SEM images of the annealed 100 nm Au bridging the implanted regions show a very non-uniform film, with the Au completely off the YBCO in areas and balling-up in other areas, as shown in Figure 7.

3.4 GAP APPROACH

In another approach to weak-link formation, we investigated the use of the FIB system to write FIB traces partially across the 5 μm YBCO lines. This approach leaves narrow gaps of superconducting material which can be driven normal by current-biasing the YBCO lines (see Figure 8). If the narrow gap is short enough (dictated by the width of damaged YBCO left by the ion beam) superconducting tunneling through the normal YBCO should occur. These experiments were done with modifications to the mask set and sample translation equipment that greatly improved sample registration, and modifications to the scan control that enabled precise placement of the unimplanted gaps.

The FIB was used to selectively damage a series of microbridges located within two unit cells on a high T_c material sample. Each unit cell made with our modified mask set had 4 single 5-μm-wide lines, and 2 patterns made with a pair of 5-μm-wide lines in parallel. The FIB implants were in the form of a single 14-μm-long line, with the capability to leave a narrow (30 to 120 nm) unimplanted gap in the center. A gapped-line writing capability was added to the FIB Microprobe pattern generator, enabling the operator to control the gap width as well as its position along the length of the line. The beam was continuously stepped by the deflection octopoles but was blanked by a separate electrostatic deflector at specific dwell positions. This yielded precise alignment of the individual segments of the line. This new beam blanking procedure eliminated a problem seen with our earlier procedure, which required a substantial delay between the time the beam was blanked and the scan restarted at the other side of the gap

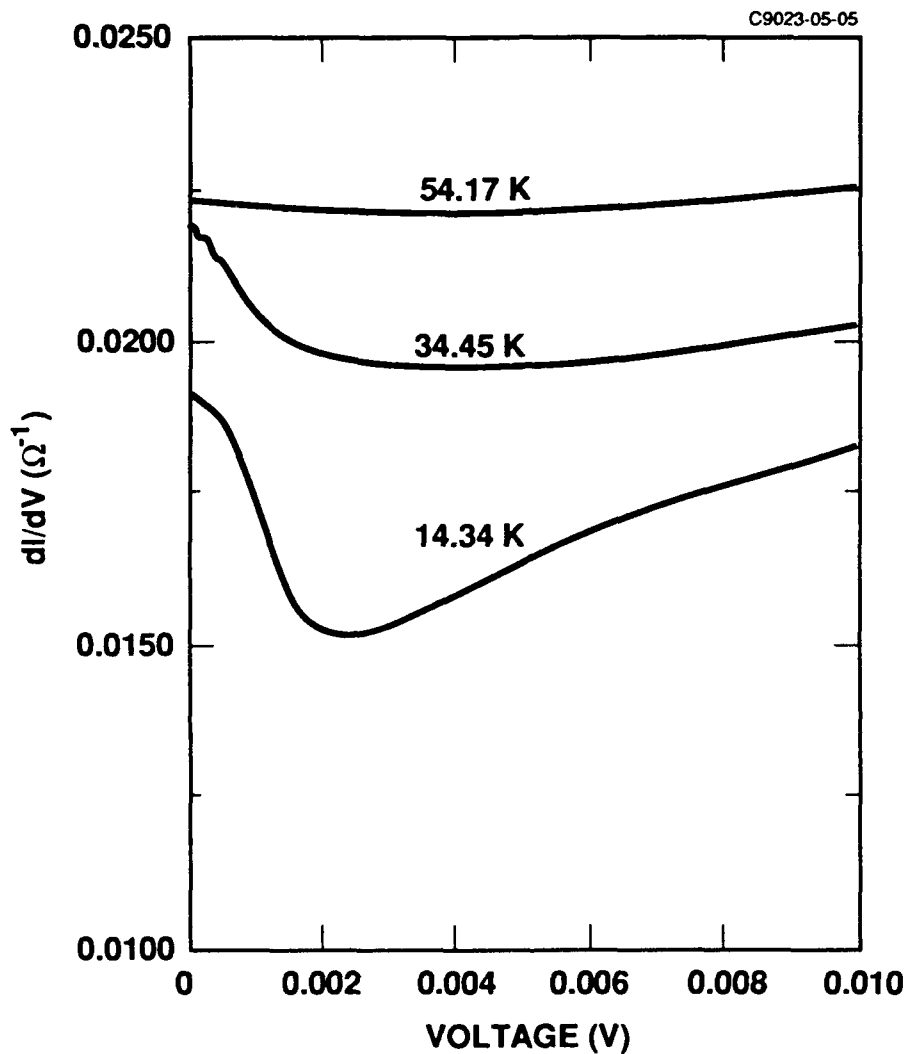


Figure 6. Conductance (dI/dV) as a function of voltage drop for the superconducting-normal-superconducting structure made with a Au bridge across a region damaged with dose of $1 \times 10^{16} \text{ cm}^{-2}$ Ga ions, showing the structure is non-linear at low temperatures, but resistive at a temperature of 54 K.

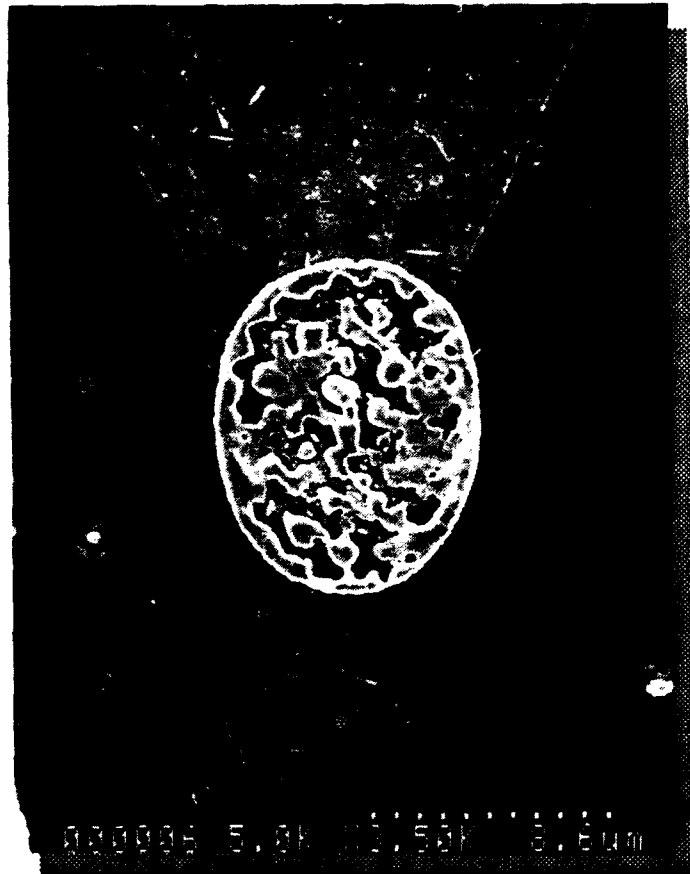


Figure 7. Scanning electron micrograph of the 100-nm-thick Au bridge spanning the damaged YBCO after a 600°C/0.5 hr anneal.

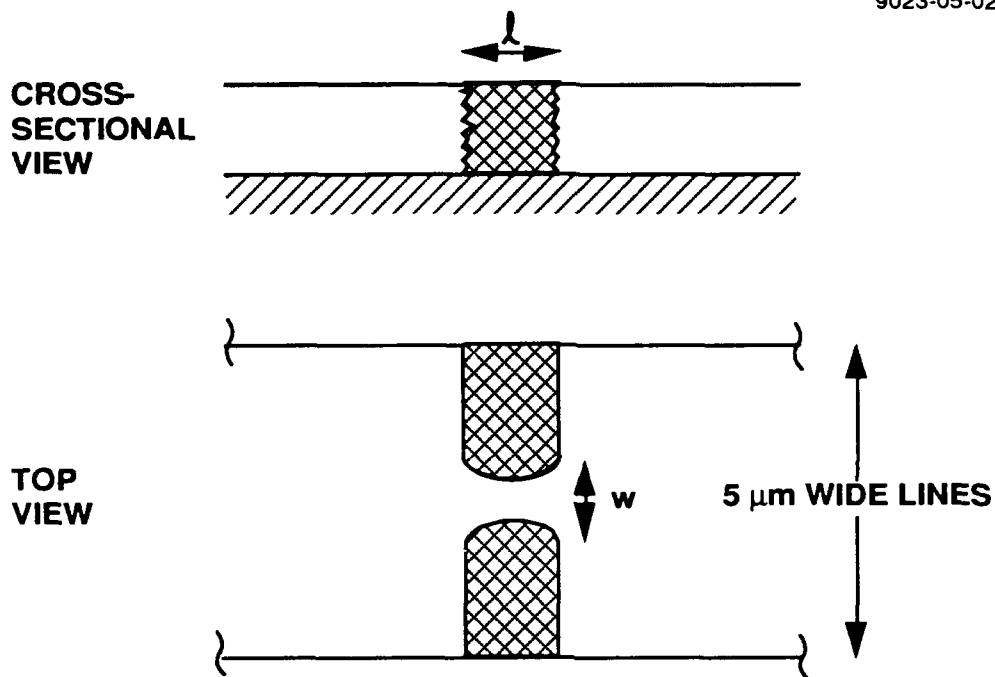


Figure 8. Cross-sectional and top views of the a procedure used to make weak links from photolithographically defined lines in YBCO. A Ga focused ion beam is used to damage the film through to the substrate. As indicated in the lower half of the figure, an undamaged gap is left near the center of the YBCO line.

(on the order of seconds). 60 Hz noise in the beam deflection optics leads to a several tens-of-nanometer uncertainty in the position of the line forming the other side of the gap. The modifications described above mean the gap is formed on the order of a few microseconds, since the noise on the deflection optics at frequencies higher than 60 Hz is negligible, and leads to a much more reproducible gap width.

We took advantage of modifications to the sample stage in the FIB system to greatly improve our alignment procedures. A precision two dimensional stage was installed (using IR&D funds) to move the sample under the beam with 0.1 μm precision, and was used to improve our registration procedure. Previously we exposed an unpatterned sample to the FIB then aligned the photolithographic masks to alignment marks made with the beam. This did not allow us to make direct before-and-after comparisons of individual devices. Our modified mask set contained metal FIB alignment marks that were used as described below. In order to locate the bridges without indiscriminately exposing the sample to the FIB, we had to access two sets of alignment marks, in "safe" areas. First, a unit cell mark was found by scanning the unit cell periphery, thus preventing damage to critical areas. The beam was then blanked and the stage was displaced a known distance to another alignment mark adjacent to a YBCO line. The beam scanned this

mark, and the stage position was adjusted slightly to center the mark relative to the scan. The stage was then displaced a known shorter distance to the first YBCO line, where a brief 5-sec raster scan verified the accuracy of the stage position (The 5-sec scan translates to a 10^{13} cm⁻² ion dosage, which produced negligible damage.) The selective implantation of each YBCO line was then accomplished, after which the second unit cell mark was located, and the procedure was repeated until all the YBCO lines were implanted.

We tested the FIB alignment procedure by using our new mask set to pattern dielectric on Si, using metal alignment marks, then using the FIB system to ion-beam sputter a cross in the center of the dielectric lines. We were able to place the crosses within 1 μ m of the center of the 5 μ m wide lines, where the alignment inaccuracy was almost entirely due to a minor misalignment of the metal FIB alignment marks to the patterned dielectric.

We started our experiments on gap formation by repeating the resistance vs. dose experiments over a more restricted range than before, and utilizing films deposited onto LaAlO₃ substrates. Furthermore, we used the new mask set described above to allow us to do a before-and-after comparison.

We deposited 3 films on 2-inch-diameter preannealed LaAlO₃ substrates -- one each 60, 90, and 120 nm thick. We cut the wafers into 1 cm² pieces, then annealed and patterned the pieces for the experiments described below. Susceptibility measurements for typical 1 cm² pieces before patterning show midpoints on the susceptibility transition between 83 and 86 K, with the midpoint monotonically increasing in temperature with film thickness.

Figure 9 shows current-voltage curves for devices from CS485C, a 60 nm film before FIB implantation. All measurements were made within 0.5 K of 49.0 K. For a 5 μ m wide bridge 60 nm thick, 3 mA represents a current density of 1×10^6 A cm⁻² (or 6 mA for the double bridges). The 0.1 μ V limit on voltage does not represent a very large electric field for the rather short bridges (~25 μ m). However, the current at which the curves reach this voltage is still close to the critical current density, since the curves are extremely flat with voltage at this point (as shown by the choice of scale: four decades for voltage and one for current).

Critical current densities for the 90 and 120 nm films without FIB damage were comparable to these: up to 1.8×10^6 A cm⁻² at 53.5 K for the 90 nm film, and up to 5.8×10^5 A cm⁻² at 72.9 K for the 120 nm film. (The thicker films were measured at higher temperatures and lower current densities because of limits on the amount of current used for the measurements.)

For the nominally 60 nm film, we did two different experiments with the focused ion beam. In the first, we wrote lines at various doses completely across 5 μ m wide YBCO bridges. The results were not consistent with the earlier results on nominally 60 nm films on SrTiO₃ substrates. Higher doses (10^{15} Ga cm⁻² and above) did not consistently render the bridges high resistance.

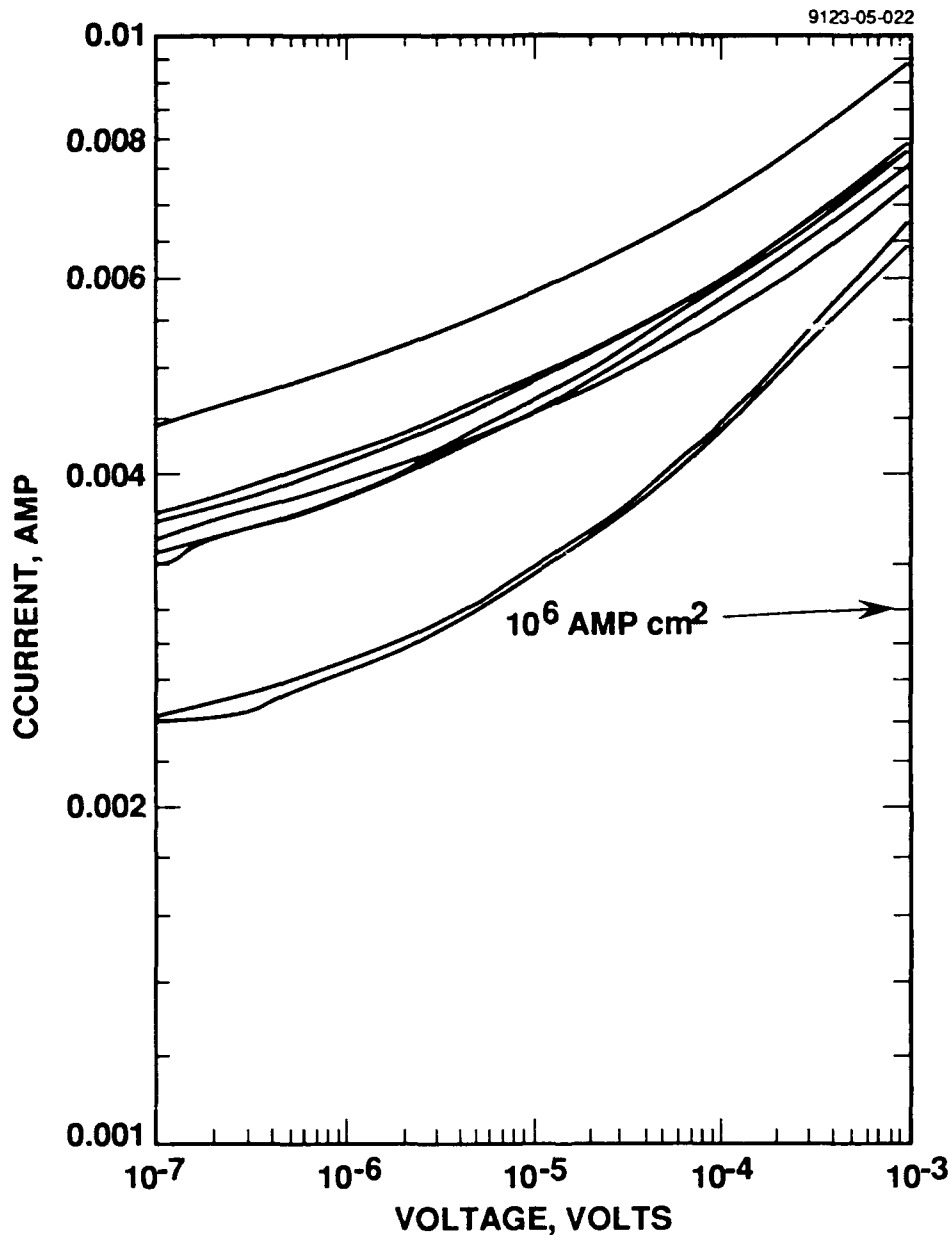


Figure 9. Current-voltage characteristics measured at 49 K for eight different $5\ \mu\text{m}$ wide lines patterned in a 60 nm thick YBCO film. A current of 3 mA corresponds to a current density of $1 \times 10^6\ \text{A cm}^{-2}$ and is indicated on the figure.

We believe that we are modifying the damaged lines during measurement, and that differences in thermal properties of the films on different substrates may be a factor in explaining the differences in the behavior between the films on SrTiO_3 and on LaAlO_3 substrates. SEM images of the bridges after FIB implantation reveal very faint, if any, traces across the YBCO.

After measurement, we often see pronounced melted regions in the area implanted with the FIB for films on LaAlO_3 substrates. We believe that the very localized damage of the FIB can lead to very localized heating during measurement. We now very carefully limit the power dissipation during our current-voltage measurements to avoid these effects.

Our second experiment with the nominally 60 nm films was to write lines across the bridges with doses of 10^{15} cm^{-2} , leaving unimplanted gaps of from 30 to 120 nm near the center of the bridges. Figure 10 shows the critical current before and after this process for a 50 nm gap. These results are consistent with the 10^{15} cm^{-2} dose not producing a high resistivity line, since the critical current should be reduced by a factor of over 100 if we restricted the current to only the gap region, rather than the observed factor of approximately 25. SEM evaluation of the implanted regions again suggests that testing modifies the implanted material, possibly allowing it to carry supercurrent in spite of the damage.

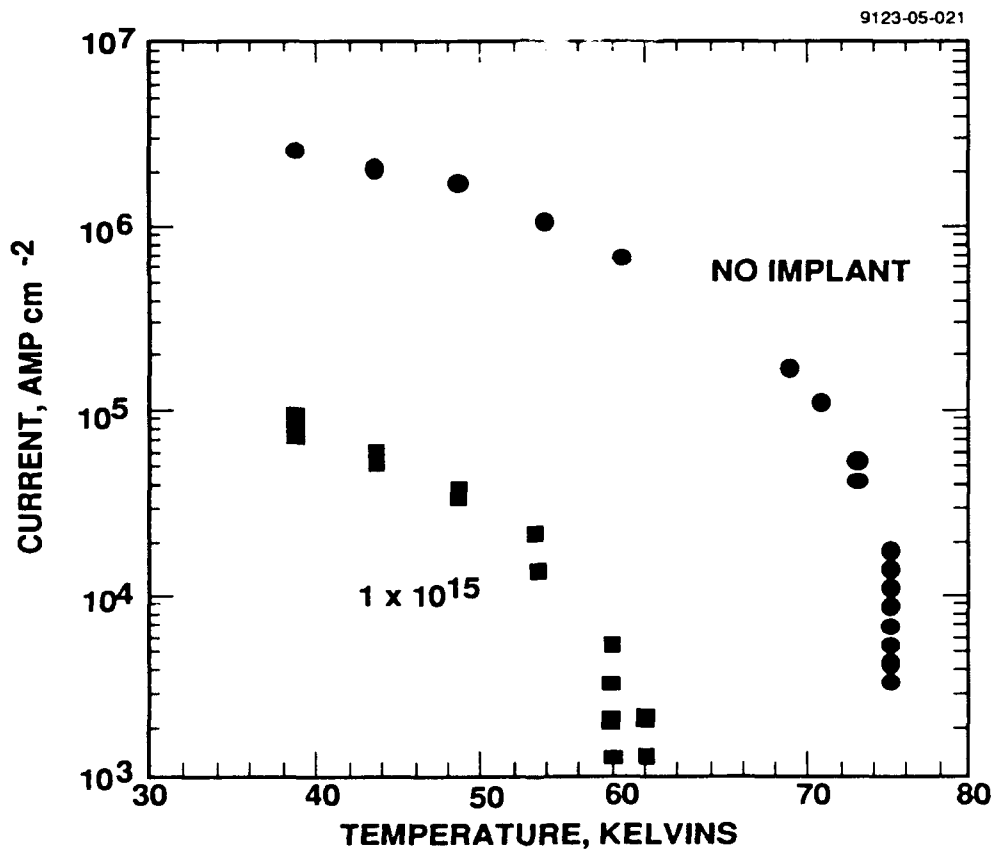


Figure 10. Critical current density for a $5 \mu\text{m}$ wide line patterned in a 60-nm thick YBCO film before (circles, upper set of points) and after (squares, lower set of points) patterning with a focused ion beam. The line was written across with a single trace of the 50 kV Ga beam at a dose of $1 \times 10^{15} \text{ cm}^{-2}$, where a 50-nm wide gap was left undamaged near the center of the line.

To more closely match the film thickness to the range of the ions used in the FIB, we used a Monte Carlo calculation (TRIM-89, written and supplied by J. F. Ziegler, IBM) to determine the range and extent of damage created by the implanted Ga-ions. Figure 11 shows the concentration of Ga as a function of depth, and the concentration of Cu vacancies. Our conclusion from this calculation is that 20 or 30 nm films would be more optimum for this energy of Ga ions than the nominally 60-nm films discussed above.

Further work was done using 20, 30, and 40 nm post-annealed films. Figure 12 shows AC magnetization for post-annealed (850°C in wet O₂ for 30 min) films grown to either 20, 30, or 40 nm. The 40 nm films shown all have transition midpoint well above 80 K, better than was achieved in the milled sample of approximately this thickness described above.

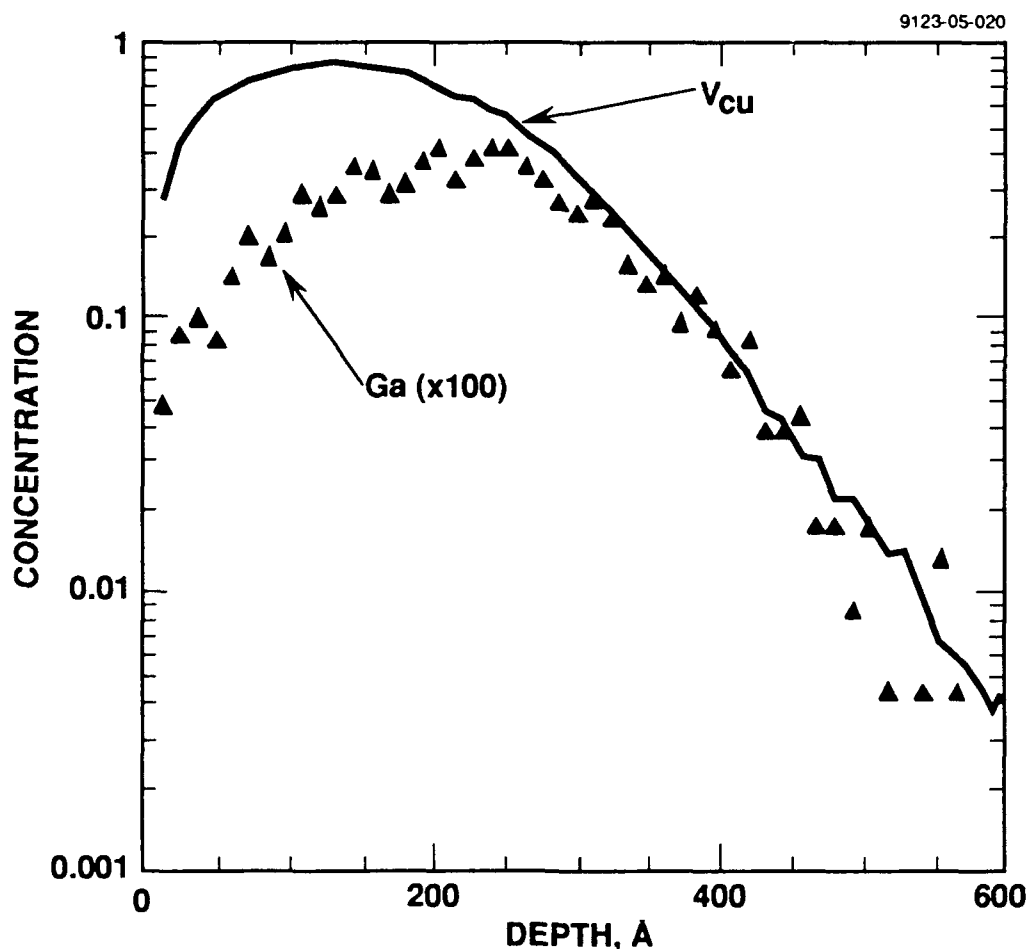


Figure 11. TRIM calculation (J. F. Ziegler, IBM) showing the concentration of Ga (triangles) as a function of depth for a 50 kV Ga ion beam in YBCO. Also shown, as a measure of the damage created by the implant, is the concentration of Cu vacancies (solid line) as a function of depth.

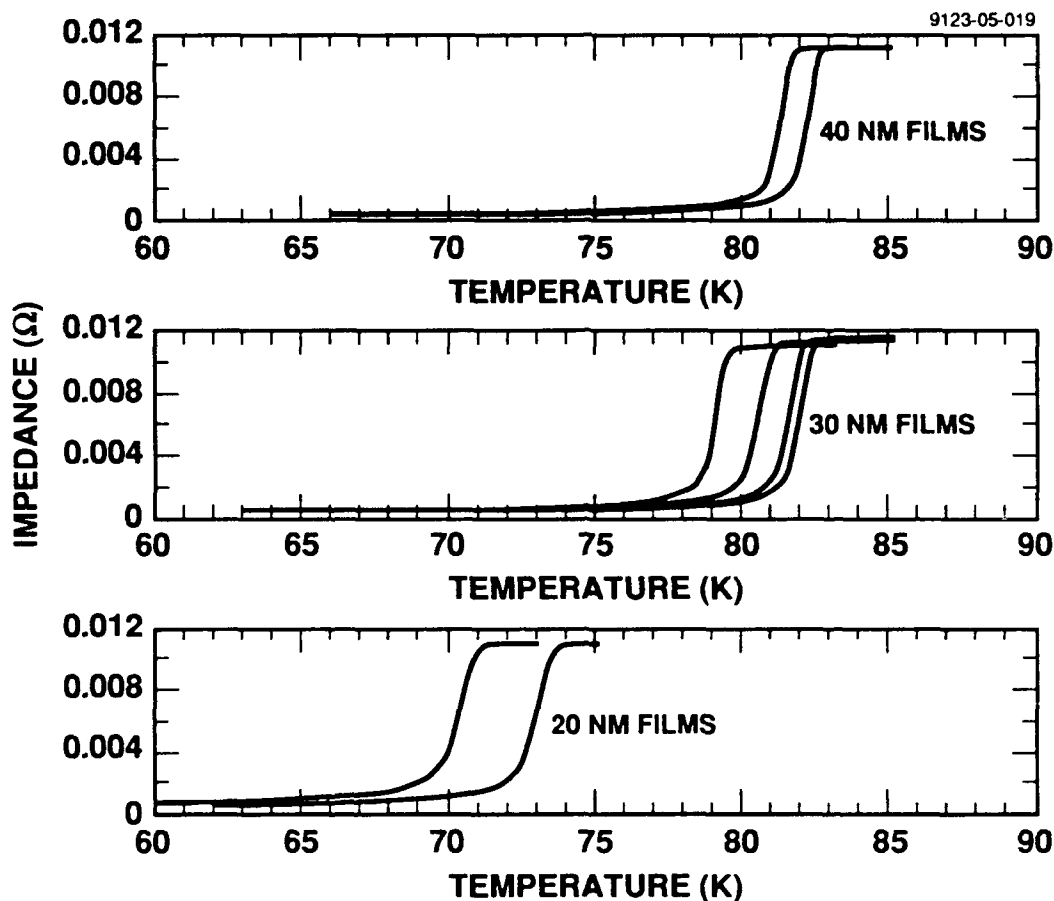


Figure 12. AC magnetization scans as a function of temperature for thin post-annealed YBCO films used for focused ion beam damage experiments. The top traces show transition temperatures for 40-nm films above 80 K, the middle traces, for 30-nm films, show transition temperatures near 80 K, and the bottom traces show transition temperatures above 70 K for 20-nm films.

We shaped the films using our SNS-3 mask set to make 5 μm wide lines that could be subsequently patterned using our Ga FIB system. Figure 13 shows current vs voltage data for six devices from CS532B, a 20 nm thick film. The film was annealed in oxygen at 500°C after patterning was complete. Two of the six devices were double bridges intended to form SQUIDS after FIB patterning, and the currents for these devices were divided by two to compare with the single bridge devices. The current densities for all six devices are very similar, with a spread of approximately $\pm 10\%$ at 19.3 K. The critical current density for this film at 19.3 K is $1.0 \times 10^6 \text{ A cm}^{-2}$, estimated from the current density at 10^{-7} V .

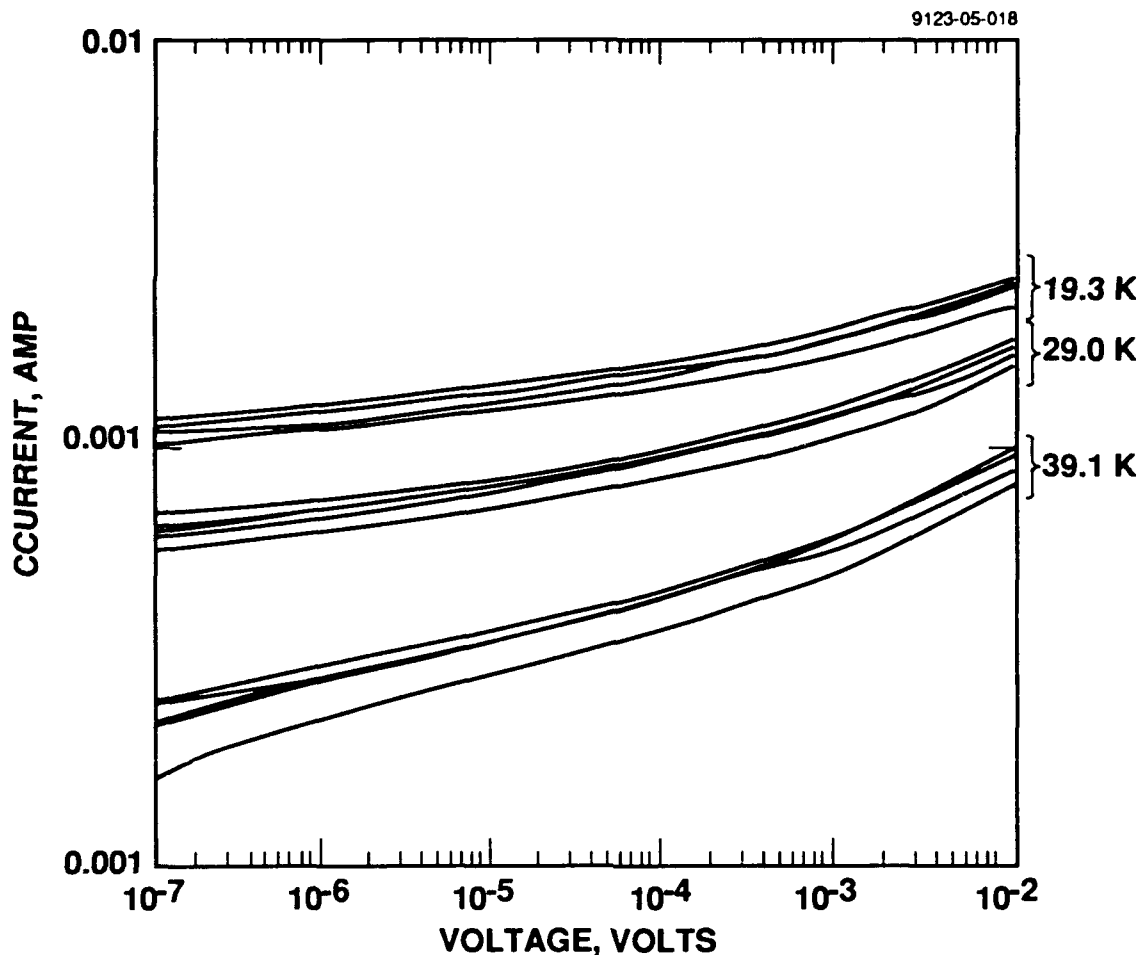


Figure 13. Current-voltage characteristics for 4 different 5- μm wide lines, and 2 devices consisting of two 5- μm wide lines in parallel, patterned from a 20-nm thick post-annealed YBCO film showing excellent uniformity and high current density before FIB exposure. (The currents for the parallel lines were divided by two to compare with the other measurements.) The top set of traces were measured at 19.3 K, the middle at 29.0 K, and the bottom at 39.1 K. A current of 1 mA corresponds to a current density of 10^6 A cm^{-2} .

We used a 50 kV, 8 nm FWHM Ga focused ion beam to write all the way across 5 μm wide lines of YBCO at doses of 0, 3×10^{13} , 1×10^{14} , 3×10^{14} , 1×10^{15} , and $3 \times 10^{15} \text{ cm}^{-2}$. For the 20 nm film, the unimplanted control device was not superconducting after the vacuum exposure, and instead had a 30 K resistance of 18 or 33 Ω (for two different devices). The resistance for all other doses was larger, rising to 175 and 4.3 k Ω for two devices implanted at $3 \times 10^{15} \text{ cm}^{-2}$. While the maximum resistance for the pairs of devices implanted at the same dose rose monotonically as dose was increased, for several of the intermediate doses, the resistance of one of the devices was lower than for the control device. We suspect this behavior may be a consequence of film thickness non-uniformity in our post annealed films

After a 500°C anneal in oxygen, the two unimplanted control devices were again superconducting, while the two devices implanted at $3 \times 10^{15} \text{ cm}^{-2}$ still had high resistances: 50 and 14000 k Ω , respectively. After the anneal, the two devices implanted at the lightest dose ($3 \times 10^{13} \text{ cm}^{-2}$) were not superconducting, and both had resistances of 2 Ω at 30 K.

The results for the 30 nm film were similar to the results for the 20 nm film, but with some importance differences. These thicker films were much less susceptible to changes in oxygen content, and therefore critical current density, than were the 20 nm films. For the 30 nm film thickness, the devices implanted at $3 \times 10^{13} \text{ cm}^{-2}$ were superconducting at 30 K after a 500°C anneal, with a reduced critical current density. The difference between pairs implanted at identical doses was more significant than for the 20 nm film. For example, while both devices implanted at $1 \times 10^{15} \text{ cm}^{-2}$ had resistances of approximately $10^5 \Omega$, one of the two implanted at $3 \times 10^{15} \text{ cm}^{-2}$ was still superconducting, although with a critical current density an order of magnitude below its pre-implant value. Again, we believe this may be due to film thickness variations which prevent the films from being uniformly damaged all the way to the substrate. This process would be more significant for the 30 than for the 20 nm films.

A complication in using these very thin films is that they are very susceptible to oxygen loss even at near ambient temperatures. This section illustrates this effect. Figure 14 shows current-voltage characteristics measured for a 5- μm -wide line from a 20-nm-thick film at 24 K at several steps after processing. The third curve from the top was measured just after processing was completed. The transition marked "1" shows the loss of superconductivity caused by vacuum exposure during SEM writing of the other bridges. Annealing the sample for 30 min in dry O₂ at 500°C improved the critical current to well above the as-processed values, as is indicated by the curve at the end of the arrow labeled as "2". Finally, a two week storage in a N₂ dry box resulted in the reduction in critical current labelled "3". The critical current density for this device at 24 K was approximately $1 \times 10^6 \text{ cm}^{-2}$ after the storage in N₂.

We believe oxygen content in the films is responsible for these variations. Slight heating encountered during certain processing steps, and during the e-beam irradiation during SEM imaging, allows oxygen to diffuse out of these very thin films into vacuum. This lost oxygen is replaced in the 500°C anneal, improving the superconducting properties of the devices. We have developed MgO "passivation" layers under our IR&D program that prevent this oxygen loss, which should make actual devices stable. During the FIB dose experiments, however, where we do not want the thickness of the passivation layer, we make transport measurements as soon as possible after a 500°C oxygen anneal.

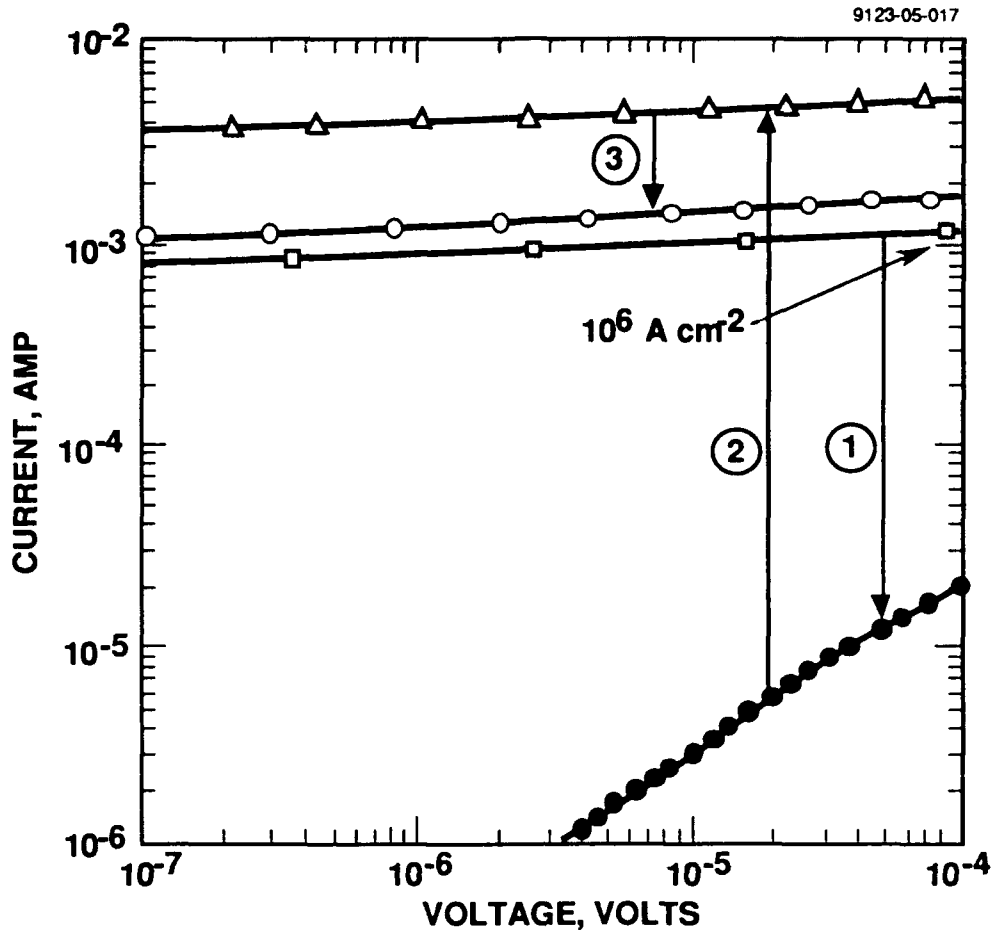


Figure 14. Current-voltage characteristics for a 5- μm wide line patterned in a 20-nm thick post-annealed YBCO film, at various stages of processing. The line marked "1" shows loss of superconductivity following vacuum exposure during FIB writing (of other lines). The line marked "2" shows the recovery of superconductivity following a 500°C anneal in O_2 , and the line marked "3" follows the reduction in critical current density caused by a two week storage in N_2 .

The morphology of the samples discussed above was limited by the presence of "boulders" of other phases and a slight basket weave surface pattern caused by the a-axis nucleation. Because the range of the very high resolution FIB was of the order of the film thickness, morphology is probably an extremely important parameter governing the reproducibility of the FIB damage. We pursued annealing experiments in an attempt to improve the thin film morphology, and did FIB dose experiments on one set of samples with improved morphology.

Previous post annealed films were made by placing the amorphous Y-BaF₂-Cu films on a cold quartz boat and sliding the boat into a furnace pre-heated to 850°C in wet flowing oxygen for 30 min followed by a furnace cool in dry oxygen to room temperature. However, better

c-axis nucleation occurs when the sample is rapidly heated to high temperatures. Our new annealing procedure involves placing the amorphous film onto a preheated boat and quickly returning the boat into a pre-heated 900°C furnace with wet flowing oxygen. After one minute the furnace is turned off and the sample allowed to cool. The bubbler to saturate the oxygen with water vapor remains on for 30 min to ensure the proper exchange of oxygen for the fluorine in the film.

The results of the new annealing procedure were films with a flat, plate-like surface structure instead of a pitted, basketweave pattern. The boulders were reduced in numbers, and were smaller and rounded instead of long and rod-like. The critical temperatures of the films were comparable to those examined previously, and the critical currents were very high. At 50 K, we measured critical current densities of 7×10^5 A cm⁻² for a 30 nm film, and 1×10^6 A cm⁻² for a 40 nm film. We then wrote with a 8 nm FWHM 50 kV Ga beam across the 5- μ m-wide lines with doses ranging from 3×10^{13} to 3×10^{15} cm⁻². After FIB exposure, a dose of 3×10^{13} cm⁻² reduced the critical current density in two devices made from a 40-nm film by about 1 order of magnitude. For a dose of 1×10^{14} cm⁻², one of two devices measured was resistive ($\sim 0.1 \Omega$), although the other was still superconducting. Each of the two devices measured for implants at higher doses was resistive. The range of resistances was substantial. For example, at the highest dose used in this experiment, 3×10^{15} cm⁻², one line had a resistance of 2 Ω , while the other had a 100 Ω resistance. Extreme care was taken during these measurements to limit the power dissipated in the lines during measurement to eliminate any chance of self annealing modifying the lines during measurement. While the reproducibility of the FIB damage is probably better than for previous experiments due to improved film morphology, we believe further improvements are needed in film morphology to reduce the variability.

4. TRILAYER RESULTS

4.1 APPROACH TO JUNCTION FORMATION

As part of our IR&D program we have developed methods to grow and pattern trilayer structures with YBCO base and counter electrodes. A key element in these structures is the ability to deposit non-superconducting YBCO by dropping the deposition temperature during *in situ* growth. Non-superconducting films formed in this fashion did not subsequently become superconducting even when heated to temperatures required for the formation of superconducting films. We determined from these IR&D studies that we could grow epitaxial trilayers, with the top and bottom layers superconducting a-axis YBCO, and the barrier a-axis oriented resistive YBCO. We are now beginning to apply these trilayer patterning techniques to films for this program.

Figure 15 shows the processing sequence worked out for the YBCO trilayers. The trilayer is deposited *in situ* without breaking vacuum. Ion milling is first used to isolate patterns from one another by etching down to the LaAlO_3 substrate. A second ion milling step that etches the counter-electrode down through the barrier is done to define mesas of various sizes. We then sputter deposited MgO as an insulator, and used ion milling to make vias through the MgO to enable us to contact the base and counter electrodes. Finally, lift-off was used to shape the Ag/Au bilayer contacts.

4.2 ELECTRONIC CHARACTERISTICS OF PROCESSED DEVICES

As part of this program, we have completed processing on 4 1 cm^2 pieces of a trilayer structure grown on our IR&D project (all pieces cut from wafer number CS522). The barrier for this sample consisted of 10 nm of non-superconducting YBCO, and was sandwiched between superconducting layers of YBCO. All layers were deposited *in situ* without breaking vacuum. The apparent critical current density of the junctions was high, and only had a measurable I_c near T_c . With this combination of high junction critical current (probably due to the relatively thin normal barrier) and large junction area (the smallest area was $15 \times 15 \mu\text{m}^2$) we believe the current-voltage characteristics we measured may be limited by the critical current of the base electrode where the current spreads from the junction into the base electrode.

For this program, we grew and processed a trilayer with a 50 nm barrier of non-superconducting YBCO. growth run CS616. A microphotograph of the sample after processing is shown in Figure 16. In addition to the junctions, we measured current-voltage characteristics for patterns on the mask that allow the critical current of either the base electrode alone (with the

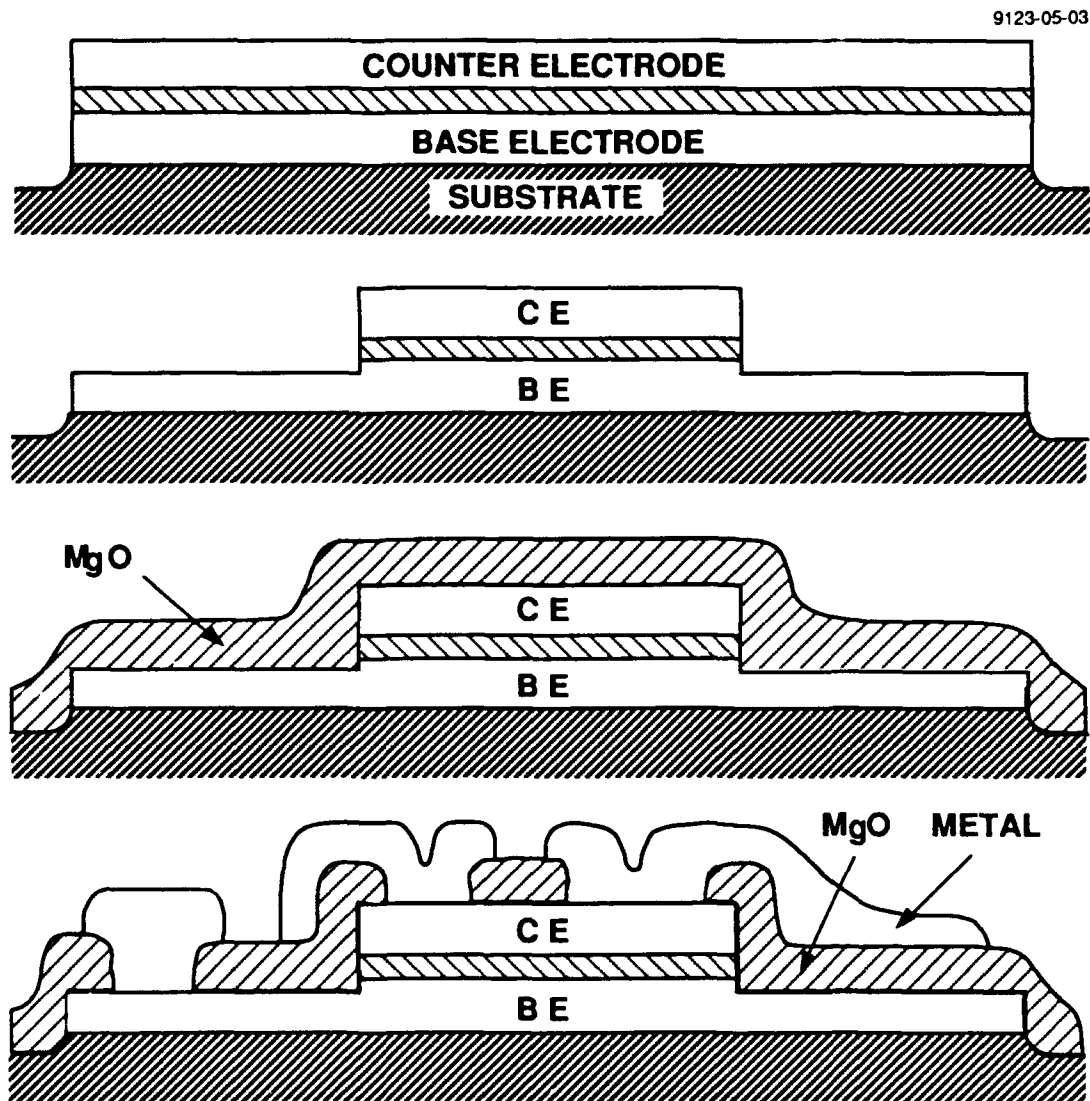


Figure 15. Diagram showing the steps taken to pattern trilayer samples into junctions. The top figure shows the trilayer after ion milling to isolate different devices. The second step is another ion mill to shape junctions of different sizes. The third figure illustrates the sample after MgO deposition. Finally, vias are milled into the MgO, then metal contacts to the base and counter electrode are shaped by lift-off.

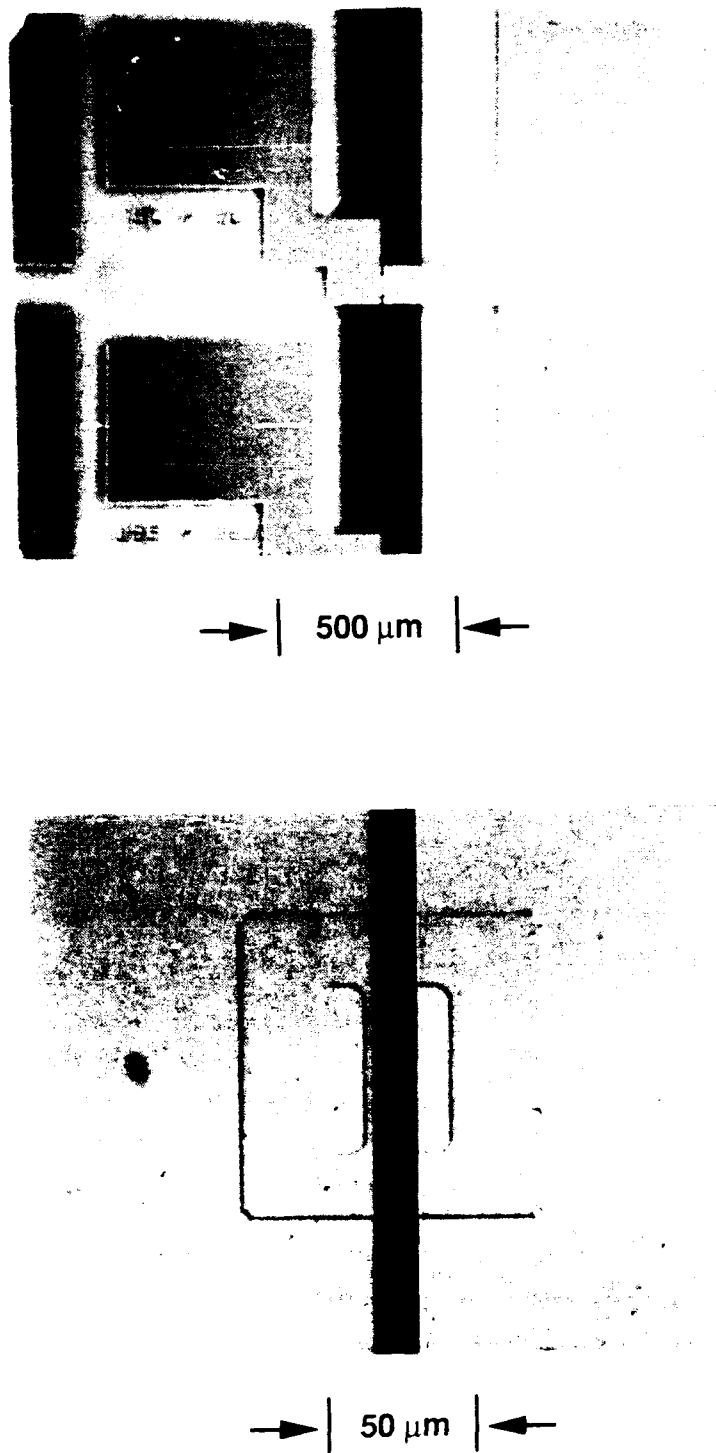


Figure 16. Microphotograph of fully processed all-YBCO trilayer junction. The left-hand picture shows metal interconnect extending from the pads to the top of the counter-electrode mesa, and the right-hand picture shows the detail of the contact to the $50 \times 50 \mu\text{m}^2$ mesa.

counter electrode and barrier ion milled away) or of the entire trilayer to be measured. Figure 17 illustrates results obtained for one set of junctions. The mesas defining the junction size were squares 15, 50, and 125 μm on a side. The critical current of the junctions, however, scaled most closely with the length of one side of the junction, instead of the junction area. This is illustrated in the figure where we plot junction critical current at 4.4 K as a function of junction length. The three points lie very nearly on a straight line through the origin. We interpret this to mean that the junction critical current in this case is limited by the critical current of the base electrode where the current spreads away from the junction into the base electrode. This interpretation is reinforced quantitatively by the magnitude of current density calculated from the junction critical current using a cross sectional area equal to the junction length times the base electrode film thickness. For the largest junction, this yields a critical current density of $1.2 \times 10^4 \text{ A cm}^{-2}$, in close agreement with that measured for the base electrode itself at 4.5 K: 1.2 or $1.4 \times 10^4 \text{ A cm}^{-2}$ for a 10 or 25 μm wide line, respectively.

The relatively low resistance of this barrier material makes diagnostic measurements difficult. In practice, it would also be difficult to fabricate devices with a normal resistance in a useful range. Therefore we decided to apply the same materials technology to a device geometry with more promise: an all YBCO edge junction.

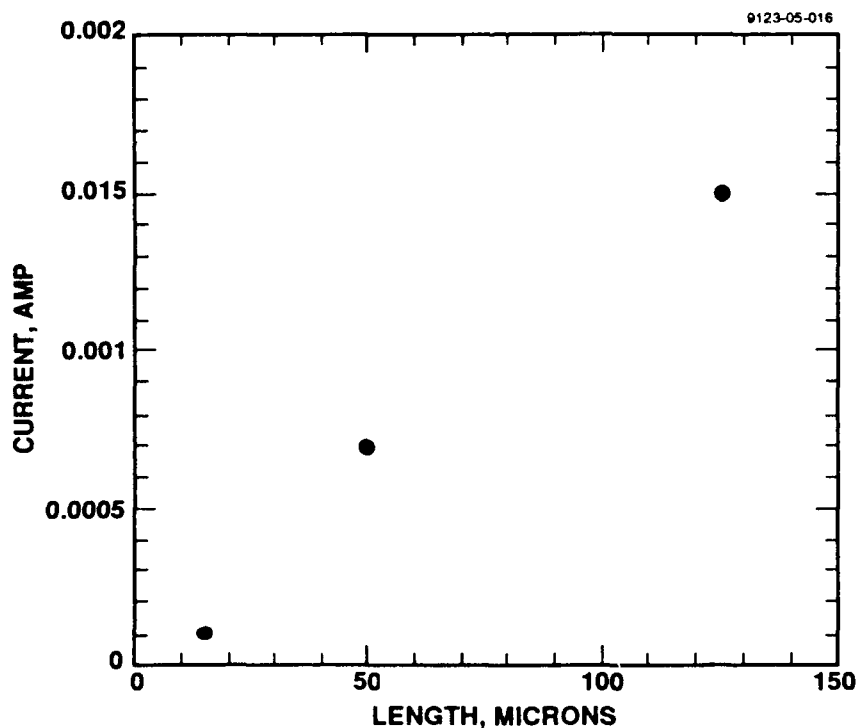


Figure 17. Critical current for three different sized trilayer junctions as a function of junction length, measured at 4.5 K.

C9023-05-03

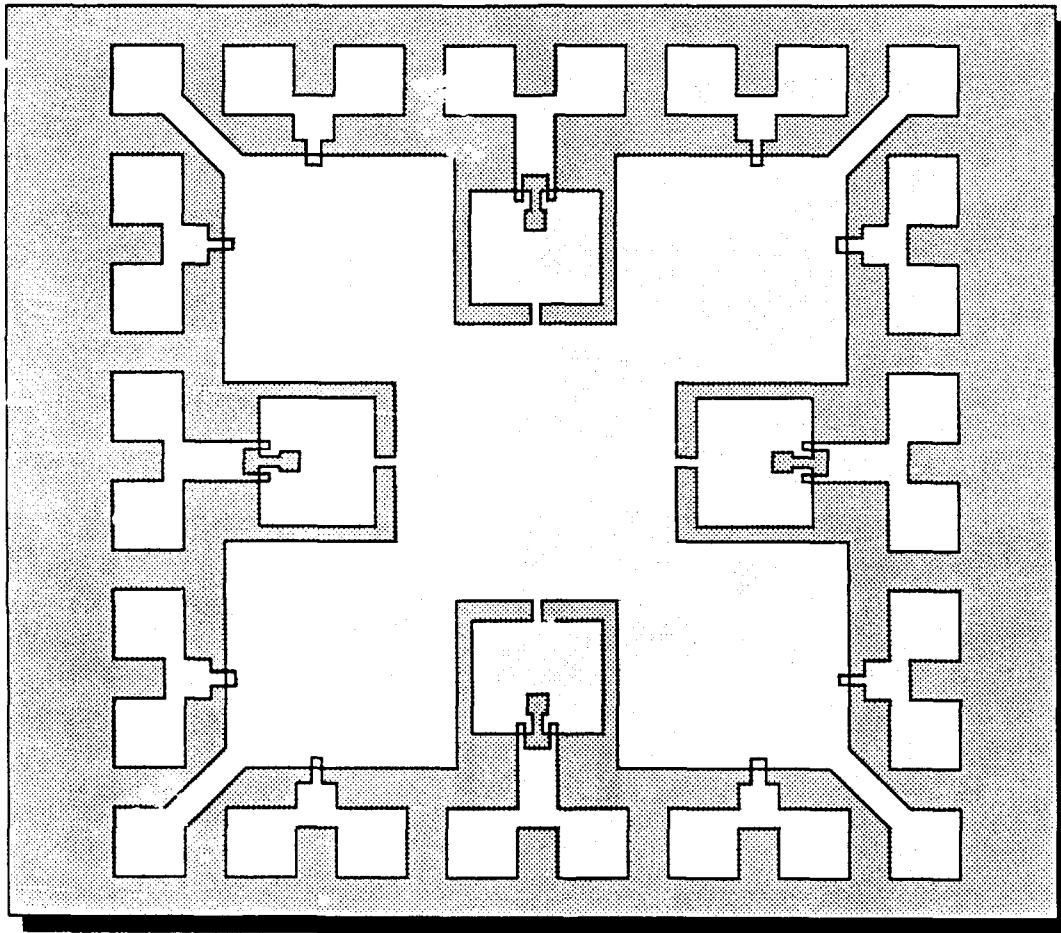


Figure 18. Diagram of one cell of the mask set used to make edge junctions from YBCO films. Single junctions of 10 and 25 μm width, and SQUIDs made with either 10 or 25 μm wide junctions, are formed by the mask set.

5. EDGE JUNCTIONS

There are several advantages of edge-junctions over trilayers, so we devoted much more of our efforts to edge junctions than trilayers. Since YBCO is anisotropic, there are substantial advantages to the edge junction geometry. All c-axis films can be used, taking advantage of the high critical current in the a-b plane for transport in the electrodes leading up to the junctions, as well as the longer a-b coherence length that helps to determine tunneling properties. Furthermore, once a single junction can be made, SQUIDs are a trivial extension in an edge junction geometry since the counter-electrode layer can be used to connect two junctions. This is not the case for trilayers: to interconnect two junctions a third level of superconductor must be deposited and shaped.

5.1 APPROACH TO EDGE-JUNCTION FORMATION

One cell of the mask set used for the photolithographic fabrication of edge junctions is shown in Figure 18. Structures included on the junction cell of the mask set include 10 and 25 μm wide single junctions, plus SQUIDs made from these junctions. A material evaluation chip was also included in the mask set to allow separate J_c evaluation for both base and counter electrodes, as well as contact resistance to both base and counter electrode. Fabrication of edge junctions requires 4 mask layers: shaping of the base-electrode and insulator, vias to the base electrode, shaping of the counter-electrode, and lift off to form normal metal contacts and bonding pads.

The processing sequence used for making the edge junctions is illustrated in Figure 19. We always used 150 to 200 nm post-annealed YBCO films for the base electrode, since these could be made quite rapidly over large areas. Approximately 200 to 250-nm-thick films of MgO were then sputter deposited over the YBCO to form a thick insulating layer. These layers were then shaped (this step defines the edge) with ion milling. In a separate step we ion milled vias to the base electrode through the MgO. The sample was then ready for barrier and counter-electrode deposition. For most runs we formed the counter-electrode using *in situ* YBCO, although in some cases we tried post-annealed material for this layer. The counter-electrode layer was also shaped by ion milling. Finally, we used a Ag/Au bilayer for contacts, which was shaped by lift off. We originally verified the mask set by processing a sample with a YBCO base electrode and a normal metal counter electrode. The left-most part of Figure 20 is a microphotograph of a fully processed all-YBCO edge junction SQUID. The darker material to the left is the MgO covered base electrode. The lighter-colored counter electrode material contacts the base electrode edge in two narrow 10- μm -wide strips. The two independent counter-electrode contacts are seen at the right side of the picture. An magnified microphotograph shows the detail of the 10- μm -wide counter-electrode line contacting the base-electrode edge.

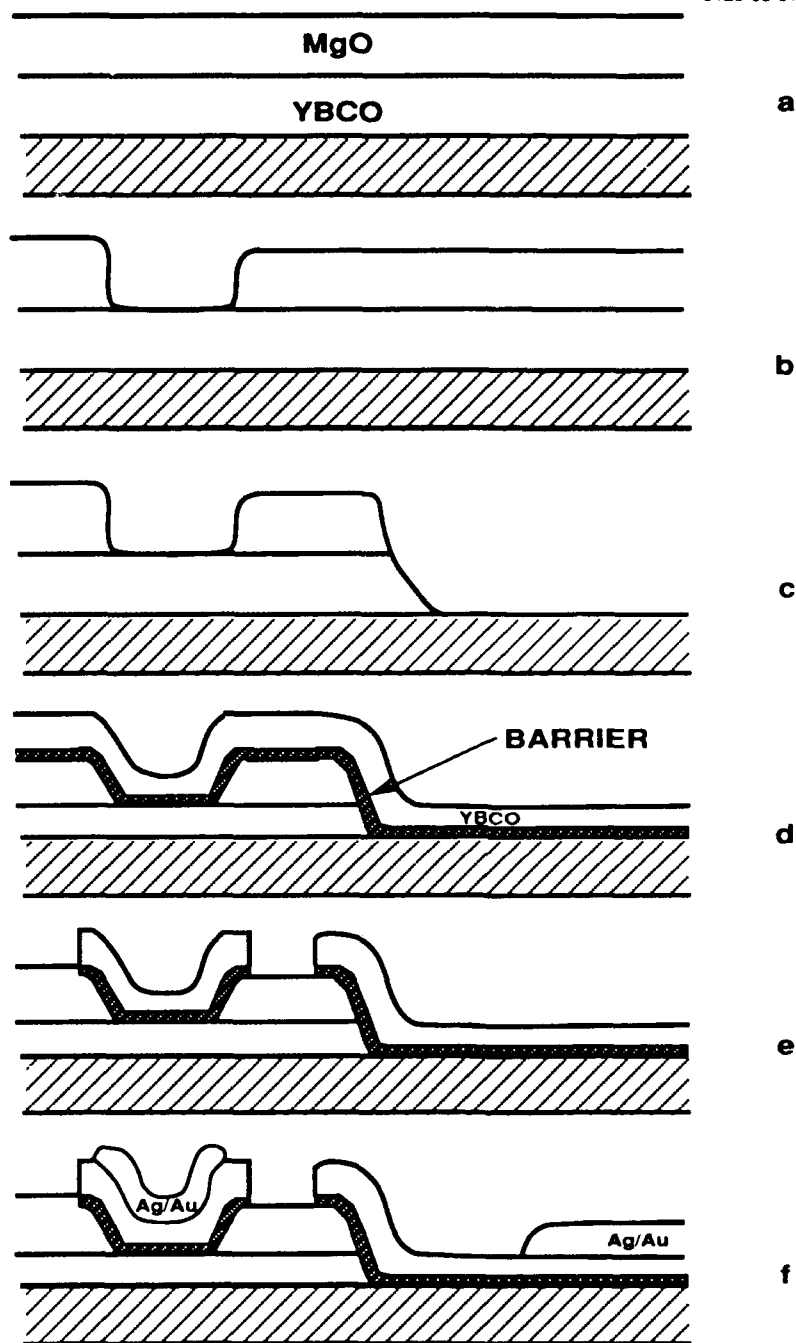
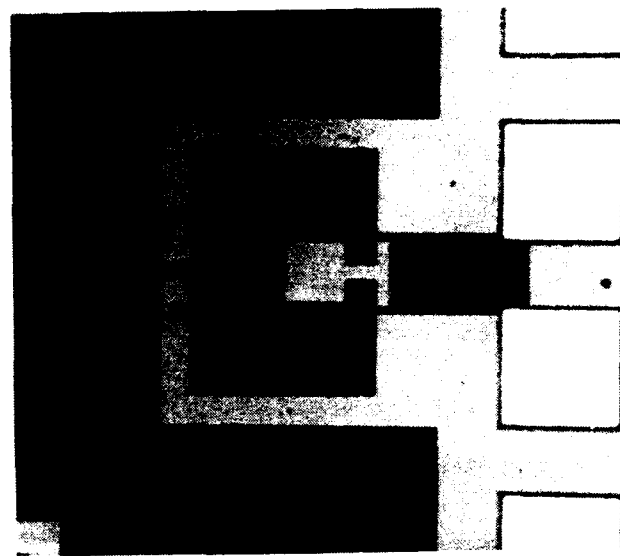
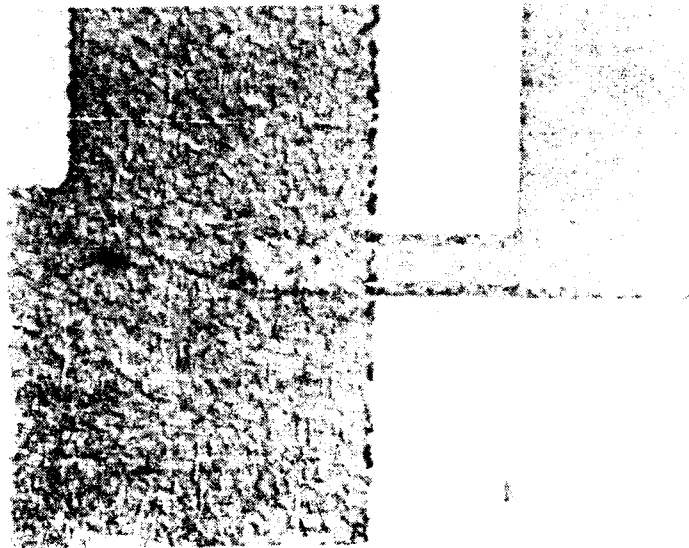


Figure 19. Diagram showing the procedure used to fabricate edge junctions from YBCO films. Post annealed YBCO films are first covered with 250-nm thick MgO films ("a"). "b" illustrates vias ion milled into the MgO for base-electrode contacts. The next step involves milling an edge into the MgO and YBCO ("c"). The barrier and counter electrode layer are deposited ("d") then shaped by ion milling ("e"). The last step is to make normal metal contacts to the base and counter electrode ("f").



→ | 200 μm | ←



→ | 10 μm | ←

Figure 20. Microphotograph of a fully processed all YBCO edge junction SQUID (left hand picture) showing details of 10- μm wide counter electrode line contacting base-electrode edge (right hand picture).

We experimented with Br-etching as a method to clean the edges after ion milling. We deposited SiO_x and Si_3N_4 on 60 and 600 nm (respectively) thick films of $\text{YBa}_2\text{Cu}_3\text{O}_7$ and patterned lines by ion milling. The edges were subsequently etched for 10 sec in 0.5% Br in ethylene glycol to remove damage created by ion milling the edges. SEM images demonstrated that the YBCO was etched out from under the dielectric by a distance of the order of ten of nanometers. Because we were concerned that the undercutting may prevent good deposition of counter-electrode material onto the edge, our actual edge junctions were fabricated without Br etching. We have evidence, discussed below, that the heating taking place during the counter-electrode deposition is sufficient to heal the ion milling damage at the edge.

5.2 DEVICE CHARACTERISTICS WITH NO DEPOSITED BARRIER

All-YBCO edge junction samples were fabricated employing post annealed material for the base electrode, and either post-annealed or *in-situ* material for the counter electrode. After deposition of the base electrode material onto two-inch-diameter LaAlO_2 substrates, the wafers were cut into quarters and annealed after cutting. MgO was deposited on each quarter processed, then the base electrode vias and edges were formed in two separate ion milling steps. CS524A and B had *in situ* material deposited for the counter electrode. Samples CS524C and D and CS539B and C had amorphous F-containing layers deposited, which were then crystallized in a post deposition anneal. No deliberate barrier was deposited for any of these initial samples. The counter electrode layer was then shaped with ion milling, and Ag/Au contacts fabricated by evaporation and lift-off. All samples were annealed at 500°C for 30 min in O_2 to replace oxygen lost during the deposition steps, and to lower contact resistance. The samples were then cut, mounted in 64 pin headers, and wirebonded.

CS524D and CS539C were formed with post-annealed counter electrodes where the counter-electrode material was annealed at 750°C (the same temperature used for the *in situ* counter electrode growth) for 30 min in 200 m torr O_2 (with the balance of the 1 atm gas in the open tube furnace made up of H_2O saturated Ar). AC magnetization of the partially processed piece in this case indicated that the counter electrode material had a broad transition starting at ~ 70 K, but not reaching 90% shielding until ~ 58 K. Current-voltage characteristics of the finished devices in this case indicated superconducting shorts between the base and counter electrodes, but the critical currents were lower than for the *in situ* counter electrodes discussed below. At 5 K, critical current densities varied widely, ranging from a few A cm^{-2} to over $4 \times 10^5 \text{ A cm}^{-2}$.

CS524C and CS539B, with counter electrodes formed with a 630°C , low O_2 partial pressure post anneal, did not exhibit a fully superconducting magnetization response after 15 h of annealing. Therefore, these structures were not processed any further.

Figure 21 shows magnetization vs temperature plots for CS524A at two stages of processing. The right-hand trace shows the transition of the base electrode material before any processing was done, indicating a T_c of 86 K, and a transition width of 0.5 K. The left hand trace is for the sample after counter electrode deposition (at a substrate temperature of 750°C) but before counter electrode patterning. For this sample an extra 500°C anneal was performed prior to the measurement to replace oxygen lost from the base electrode during MgO deposition and/or counter electrode deposition. The transition temperature of the *in situ* counter electrode is approximately 66 K. The patterned base electrode still provides a small degree of shielding up to 86 K where this layer becomes normal, accounting for the small step between 86 and 87 K.

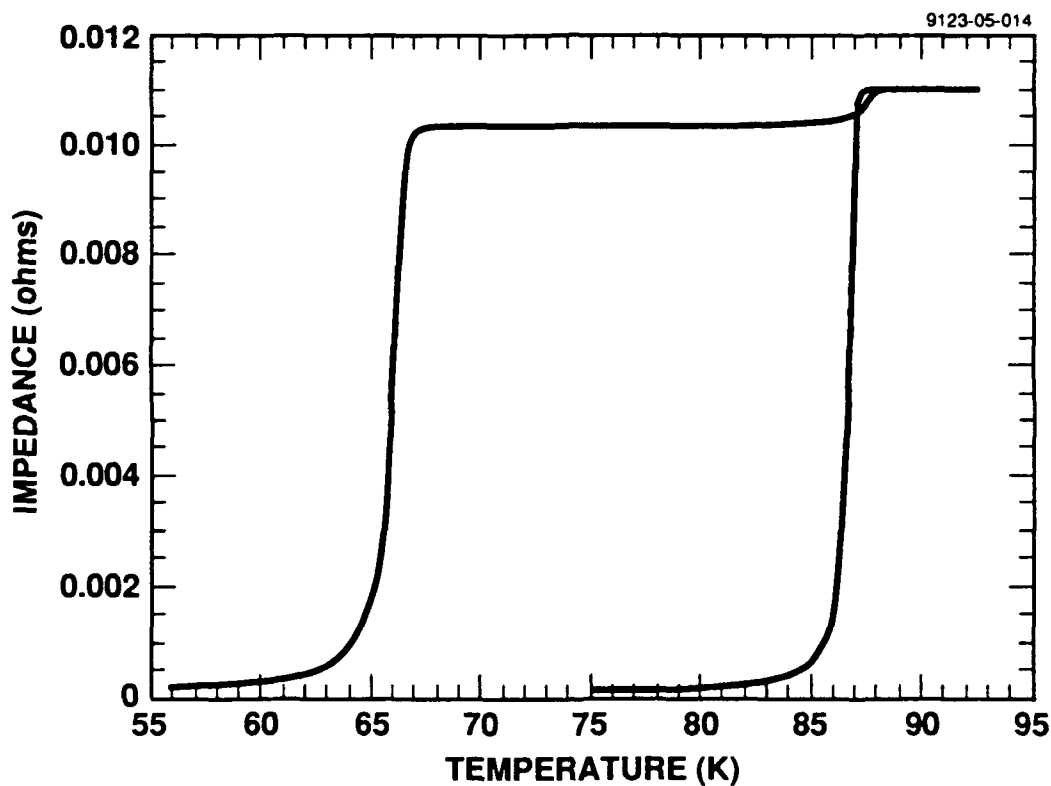


Figure 21. AC magnetization as a function of temperature for an edge junction sample. The right hand trace was measured on the base-electrode before patterning, and shows a transition temperature of ~86 K. The left hand trace was measured after counter electrode deposition, and shows a counter electrode transition temperature of ~67 K. The small change in shielding at 87 K occurs at the transition temperature of the patterned base electrode.

Current voltage measurements between the counter and base electrode of CS524A indicate a superconducting short through the edge. Critical current densities through junctions formed by contact between the base electrode edge and either 10 or 25- μm wide lines in the counter electrode vary between 3 and $9 \times 10^5 \text{ A cm}^{-2}$ at 40 K. For one 10 μm device with a 40 K critical current density of 3×10^5 , a critical current density of $1.4 \times 10^6 \text{ A cm}^{-2}$ was measured at 14 K. At 60 K, the critical current density for the tested structures varied between 1 and $6 \times 10^3 \text{ A cm}^{-2}$. The critical current density of the junctions is probably limited by the critical current density of the counter-electrode layer. This can be seen from Figure 22, where the critical current density of the counter electrode at 40 K is just above 10^5 A cm^{-2} , and drops to zero above 50 K. Since no barrier was placed between the base and counter electrode, this result demonstrates successful processing of all the other elements needed to form edge junctions. The critical current density of the post-annealed base electrode after complete device processing is excellent, exceeding $1 \times 10^6 \text{ A cm}^{-2}$ at 67 K. The *in situ* counter-electrode, although it has a low critical temperature probably due to a slightly non-stoichiometric composition and a lower than optimum deposition temperature, has a very good critical current density, exceeding $1 \times 10^6 \text{ A cm}^{-2}$ below 20 K. This result also has important implications for superconducting interconnects, since the connection between the base and counter electrode allows such high current densities.

5.3 DEVICE CHARACTERISTICS WITH DEPOSITED BARRIER

We performed several further deposition runs that used non-superconducting YBCO barriers under the counter electrode. Four two-inch wafers were prepared with 150 nm post-annealed base electrodes. The base electrodes for these experiments were annealed at 850°C in 20 Torr of O_2 in H_2O saturated Ar, which we have determined from an IR&D sponsored study to lead to improved properties over our previous standard anneal for BaF_2 containing films: 850°C for 30 min in 1 atm of H_2O saturated O_2 . Figure 23 compares AC magnetization for CS524A with that from CS611A, annealed with this new procedure. The new annealing procedure leads to a higher (~91 K) and sharper ($< 0.3 \text{ K}$ for 10% to 90% shielding) transition for the film.

An additional annealing step was found to be necessary prior to the barrier layer formation to produce a counter electrode with good crystallinity. The reason for this was the presence of the ion milled LaAlO_3 that formed the template for the barrier and counter electrode deposition. In the experiment above, where no barrier was employed, the growth was initiated at 750°C, apparently high enough to anneal out the ion-milling damage and allow a high quality YBCO film to be formed. The barrier layer, however, is formed by deposition at a reduced temperature

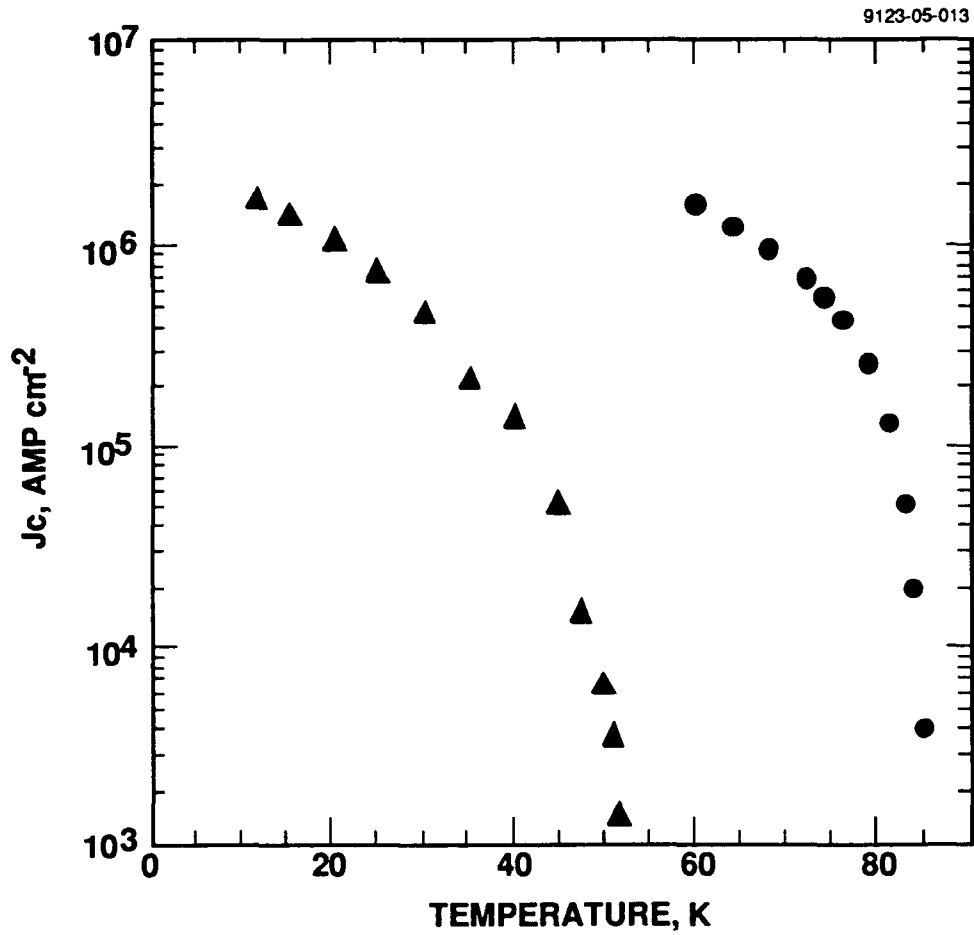


Figure 22. Critical current density as a function of temperature for test patterns fabricated from the edge junction mask set made from the base-electrode material (circles) or the counter-electrode material (triangles).

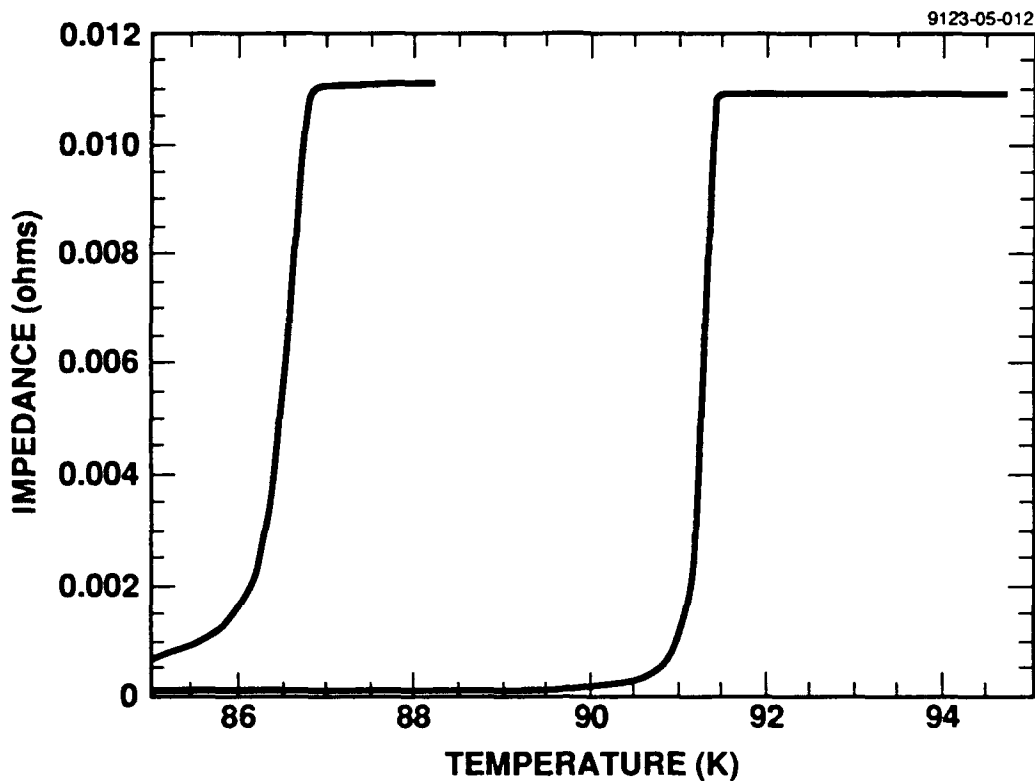


Figure 23. AC magnetization as a function of temperature for two post-annealed YBCO base-electrode layers. The left-hand trace, with the lower critical temperature (~ 86 K), was measured on a film annealed in 1 atm wet O_2 anneal, while the right hand trace with a higher 90 K transition temperature was for a film annealed at a reduced oxygen partial pressure.

(between 500 and 550°C). While this does not present a problem when the barrier is deposited onto an unmilled substrate, the ion milling damage prevents oriented growth of the barrier layer from occurring. The sequence successfully used for the formation of a non-superconducting YBCO barrier and superconducting counter-electrode includes an initial temperature ramp to $\sim 750^\circ\text{C}$. The substrate temperature is then reduced to 500°C before the target shutters are opened and growth is initiated. After the barrier growth is completed, the temperature is ramped to 750°C for the counter-electrode deposition.

Sample CS614A has a base electrode similar to CS611A described above, and was fully processed into edge junctions. All steps leading up to the barrier and counter electrode formation were as described above for CS524A. The barrier and counter electrode were deposited using the pre-annealing procedure explained in the preceding paragraph. A 10 nm non-superconducting YBCO barrier was deposited; then a 140 nm counter-electrode layer was deposited. The sample

temperature anneal of the sample in oxygen to make up any oxygen deficiency due to the rapid cool down. Figure 24 shows an AC magnetization measurement on the sample after this low temperature anneal and prior to counter electrode shaping. While the transition temperature of the counter-electrode is somewhat low (approximately 48 K, probably due to being slightly non-stoichiometric) the film is fully superconducting. We were unable to obtain a superconducting counter electrode on top of the non-superconducting barrier without the pre-annealing step used for this sample. The base-electrode transition temperature after this processing is approximately 86 K, as estimated from the small step in the left-hand trace at this temperature, slightly less than the 90 K measured on the unprocessed base-electrode film (right-most trace on the figure).

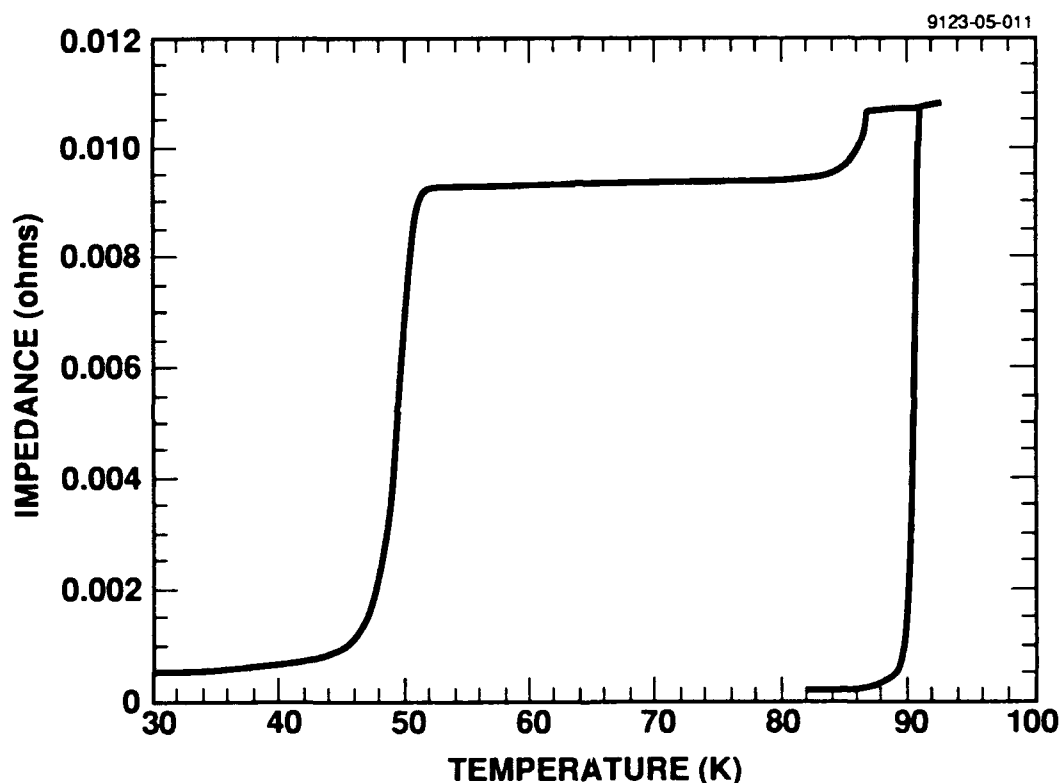


Figure 24. AC magnetization as a function of temperature for an edge junction sample at two stages of processing. The right-hand trace is for the base electrode before processing. The left-hand trace was measured after barrier and counter-electrode deposition, and demonstrates a superconducting counter-electrode layer (with a T_c of ~ 48 K) was deposited on top of a 10-nm-thick layer of non-superconducting YBCO. The superconducting transition of the patterned base electrode causes the small change in shielding of the sample seen at ~ 86 K.

After processing, critical current densities of the counter electrode and junctions were measured to determine if the junction current density was reduced by the presence of the barrier layer. Figure 25 shows that this is the case. At 10 K, the critical current density of the counter electrode is approximately 5×10^4 A cm⁻², as determined by either 10 or 25 μ m wide lines. The critical current density for a typical edge junction is also shown, and is less than 1×10^4 A cm⁻² at 10 K.

We exposed the weak link junctions from this sample to radiation in the range 1 to 8 GHz. In many cases the critical current density of the junctions could be reduced to zero by the application of this RF radiation. However, we were unable to observe steps in the current-voltage characteristics at voltages corresponding to $hf/2e$ (where h is Planck's constant, f is the frequency, and e is the electron charge).

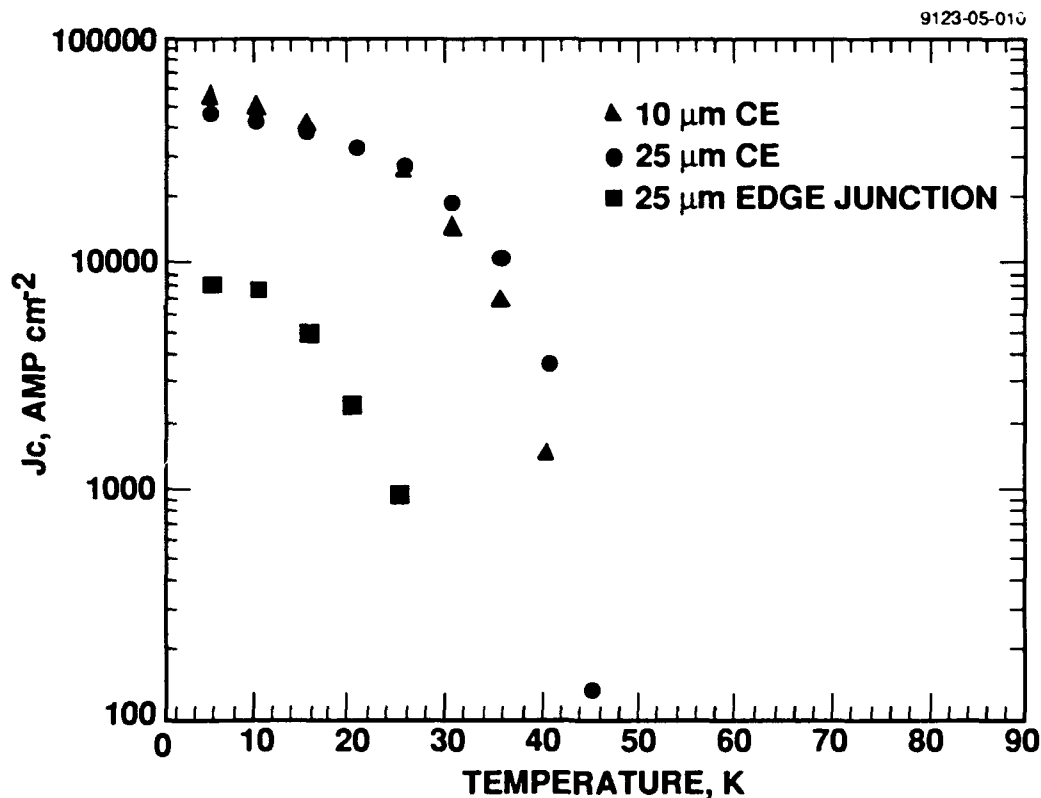


Figure 25. Critical current as a function of temperature for patterns on an edge junction sample made with a 10-nm non-superconducting barrier and a 140-nm *in situ* counter electrode. The triangles and circles are data for 10 and 25- μ m-wide lines in the counter electrode material, while the squares are data showing a much lower current density measured for a 25- μ m-wide edge junction.

6. SUMMARY AND CONCLUSIONS

In summary, we developed processes for the sputter deposition and device fabrication of Josephson tunneling structures made from YBCO materials. Very high critical current density YBCO films were used to make several different types of weak link structures, including FIB damaged YBCO lines, trilayer junctions, and edge junctions.

Post annealed thin films used in this program have excellent transport properties, with transition temperatures exceeding 90°K and with transition widths (defined as the 10 to 90% shielding transition in an AC magnetization experiment) of less than 0.3°K. Critical current densities for post annealed films routinely exceed 10^6 A cm⁻², in some cases reaching this value above 77°K. We successfully grew and patterned post-annealed films as thin as 20 nm with critical current densities as high as 3×10^6 A cm⁻² at 24°K.

The past-annealed films were used for FIB-damaged weak links and for the base-electrode layers of edge junctions. For structures involving multiple YBCO layers we used *in situ* growth (YBCO layers crystallized during deposition) because it provides smoother films and superior control of film interfaces.

The best *in situ* films used for this program had critical current densities in excess of 10^6 A cm⁻² below 20°K (measured for the counter electrode layer of an edge junction sample). The transition temperatures for most of the *in situ* films used in this program varied between 50 and 60°K -- considerably lower than for the post annealed samples. In related IR&D work, we were able to deposit single *in situ* films that had transition temperatures as high as 86°K, showing the potential of the sputtering technique. High substrate temperatures and good control of film stoichiometry appear to be the crucial factors in achieving high critical temperatures in our *in situ* films. The use of the pyrolytic BN coated graphite heater in combination with an effective infrared absorber on the back of the LaAlO₃ substrates enabled us to achieve adequate substrate temperatures with our rotatable sample stage. Precise control of stoichiometry for our *in situ* films was challenging with our three-target sputtering approach, primarily because of difficulties in accurately measuring the stoichiometry. Adequate control of stoichiometry requires calibration using RBS analysis of films grown at low temperature, then further adjustment of primarily the copper content based on film morphology and transition temperature. Extensive recalibration was required after venting the system to air. The advantages of the sputtering technique include uniform deposition over large areas, and relatively high growth rates; the primary disadvantage is the difficulty in reproducibly obtaining the required stoichiometry.

We concluded that direct writing into thin YBCO films using implantation damage is a promising method of utilizing the extremely high resolution of a 8-nm-diam focused ion beam to

pattern YBCO. We observed non-linear current voltage characteristics for superconducting-normal-superconducting structures made by bridging heavily implanted (10^{15} cm^{-2}) damage tracks with gold. For very thin films (20 to 40 nm, matched to the range of 50 kV gallium in YBCO), lower doses were sufficient to alter the transport properties. We were able to reduce critical currents with a single pass of the beam at doses below 10^{14} cm^{-2} for a 40-nm-thick film, and make the material resistive at this dose and above. Alignment procedures were developed that allowed us to write damage tracks across lines of YBCO, leaving narrow gaps (tens of nanometers across) of unimplanted YBCO in the center of the lines, an enabling technique for the fabrication of superconducting-normal-superconducting structures made by current-biasing the YBCO gap into its normal state.

We believe, however, that considerably more work would be necessary to make the FIB damage procedures reproducible. One limitation was self annealing of the implant damage during testing due to the extreme localization of the damage and therefore of power dissipation during current transport. Another contributor to the lack of reproducibility is the thickness non-uniformity of the post annealed films used for the FIB experiments. Due to the limited range of the 50 kV Ga ions in YBCO, irregularities in the film thickness of only a few tens of nanometers would shield the material below and prevent uniform damage to the substrate. This beam acceleration voltage was used because of the very high resolution it afforded: the 8-nm beam diameter is the highest resolution beam available, and the low energy of the ions and the thin films also meant the resolution was not degraded by lateral straggle of the ions traveling through the material. Further refinement of this technique as a processing tool requires the use of very planar *in situ* films.

We successfully fabricated all-YBCO trilayer structures that utilized non-superconducting YBCO barriers. For either 10- or 50-nm-thick barriers, we found that the structure critical current was limited by the current density of the base electrode layers rather than that of the junction. This was largely a consequence of the device geometry and the relatively low barrier resistance provided by non-superconducting YBCO. The a-axis orientation of the structures may have limited the critical current in the base electrode as well. A need for a trilayer barrier with a higher resistivity than we can achieve with non-superconducting YBCO is indicated by these results. Developing such a material that allows the epitaxial trilayers achieved with non-superconducting YBCO represents a considerable challenge.

Edge junctions are the most promising of the devices investigated in this program. In this geometry, all transport and tunneling occur in the plane of the substrate. With c-axis films, we then take advantage of the higher critical current direction and the longer coherence length direction of the anisotropic YBCO. Furthermore, the edge-junction geometry is more favorable for low resistance barriers because the junction area can much more easily be made small than

for trilayer junctions, and edge-junction SQUIDs can be made without additional interconnect levels.

We designed an edge junction mask set, developed the processing tools necessary to fabricate YBCO edge junctions, and processed several lots of all YBCO edge junctions. For parts made with no deliberate barrier, we achieved junction critical current densities at or above 10^6 A cm⁻², limited by the *in situ* counter electrode transport properties. This result demonstrates that we have all the processing tools required for edge junction fabrication, and indicates successful annealing of the ion milling damage at the base-electrode edge during the counter-electrode deposition. This result indicates that barriers are not an uncontrolled artifact of the processing, and is a crucial test of the feasibility of making deliberate barriers with controlled properties.

The final edge-junction structures fabricated for the program utilized a 10-nm-thick non-superconducting YBCO barrier under the counter-electrode layer. An *in situ* annealing step prior to the low substrate temperature barrier deposition was essential to heal the ion milling damage of the LaAlO₃ substrate and allow proper nucleation of the barrier and counter-electrode layer. Junction critical current densities in this case were substantially reduced from those measured for the counter electrode, indicating successful fabrication of weak links. The junctions showed substantial critical current suppression on exposure to RF frequencies, another indication of the successful demonstration of an all-YBCO tunneling device. These results demonstrate the feasibility of fabricating edge junctions by co-sputtering YBCO on 2-in-diameter LaAlO₃ substrates. More optimum device behavior requires finer control of the counter-electrode stoichiometry, which could be achieved in the co-sputtering system with additional development and practice.

GLACI: BD1D
Reference No.: G4663A

R & D STATUS REPORT

FISCAL STATUS ATTACHMENT

CONTRACT NO.: N00014-88-C-0667
PROJECT NO.: 1114SS
CDRL NO.: A001

AMOUNT CURRENTLY FUNDED TO Completion \$1,700.0

ITD EXPENDITURES & COMMITMENTS FOR QUARTER	25-OCT-91	\$1,675.4
--	-----------	-----------

ESTIMATED FUNDS REQUIRED TO COMPLETE WORK \$24.6

COMMENTS: